Spring 2010

Finite strain studies of single crystal Fe3P under high pressures

John William Howard
University of Nevada Las Vegas

FINITE STRAIN STUDIES OF SINGLE CRYSTAL Fe_3P UNDER HIGH PRESSURES

by

John William Howard

Bachelor of Science
University of Nevada Las Vegas
2007

A thesis submitted in partial fulfillment
of the requirements for the

Master of Science Degree in Physics
Department of Physics
College of Sciences

Graduate College
University of Nevada, Las Vegas
May 2010

UNIVERSITY OF NEVADA LAS VEGAS

THE GRADUATE COLLEGE

We recommend the thesis prepared under our supervision by

John William Howard

entitled

Finite Strain Studies of Single Crystal Fe_3P Under High Pressures

be accepted in partial fulfillment of the requirements for the degree of

Master of Science Physics
Physics and Astronomy

Lon Spight, Committee Chair

Oliver Tschauner, Committee Member

Michael Pravica, Committee Member

Adam Simon, Graduate Faculty Representative

Ronald Smith, Ph. D., Vice President for Research and Graduate Studies
and Dean of the Graduate College

May 2010

ABSTRACT

Finite Strain Studies of Single Crystal Fe_3P Under High Pressures

by

John William Howard

Dr. Lon Spight, Examination Committee Chair
Professor of Physics
University of Nevada, Las Vegas

Fe_3P (synthetic schreibersite) is a phosphide occurring in iron alloys. Phosphorous is often considered an undesired impurity causing brittleness. Conversely, in some cases the addition of iron phosphides to certain materials is beneficial (e.g.properties of certain frictional materials are enhanced). In terrestrial rock, we do not find Fe_3P, although $(Fe;Ni)_3P$ (natural schreibersite) is found in nearly all iron-containing meteorites. In this project, we examine the unit cell parameters of Fe_3P as function of pressure and derive the respective axial and bulk compressibilities. Both Vinet and Birch-Murnaghan formulations were used to relate pressure and unit cell volume, and a comparison of each prediction was made. Comparing to independent data collected up to 62 GPa, no structural phase transitions were observed, and the sample remained in a strained state after relieving applied pressure.

TABLE OF CONTENTS

LIST OF FIGURES

LIST OF TABLES

ACKNOWLEDGMENTS

I would like to thank the late Dr. Malcolm F. Nicol for interesting me in the field of high pressure science, as well as giving me the great opportunity to do research in this field. I would like to thank my advisor Dr. Oliver Tschauner for the tremendous amount of time spent guiding me through the data analysis and writing processes. I would like to Stanislav Sinogeikin for teaching me the fundamentals of diamond anvil cells, and for introducing me to the work performed at the 16 ID-B beamline. I would also like to thank my committee members for supporting this work. Thanks to HiPSEC, HPCAT, and the UNLV staff for all of the assistance over the years. Thanks to all my fellow colleagues in the physics department, you all have been a great help. I am also greatly indebted to my parents who made it possible for me to pursue a professional career. Their love and support made me the person I am today and I am extremely grateful to have them as parents.

All experimental work was carried out at the 16 ID-B beamline of the Advanced Photon Source at Argonne National Laboratory. This work was supported by the U.S. Department of Energy and National Science Foundation.

CHAPTER 1

INTRODUCTION

In synthetic iron alloys, phosphorous is often considered an undesired impurity causing brittleness [1]. Conversely, in some cases the addition of iron phosphides to certain materials is beneficial (e.g. properties of certain frictional materials are enhanced) [1, 2]. In terrestrial rock, we do not find Fe_3P, although natural schreibersite, $(Fe, Ni)_3P$, is found in nearly all iron-containing meteorites. Meteoritic $(Fe, Ni)_3P$ has an identical crystal structure to that of synthetic Fe_3P [3], therefore we expect many similarities in chemical and physical properties between the two species.

Under proper high temperature conditions and stoichiometric proportions, synthetic schreibersite (Fe_3P) can be produced using direct capsule synthesis (a catalyst for solid diffusion) [1]. One can do this by placing correct proportions of iron and phosphorous powders into a cylindrical compact, subjecting to high temperatures ($\sim 1200K$) within a sealed quartz capsule, and annealing for $\sim$ 30 days. After the first annealing, one can further homogenize the sample by milling the contents and performing another annealing process. It has been shown [4] that the room temperature crystal structure of Fe_3P assumes space group $I\bar{4}$. Similarly, crystalline Ni_3P assumes the same space group, but with uniformly smaller unit cell parameters [5].

Equations of state are known to be extremely valuable to scientists in many different fields, most notably those pertaining to the engineering, chemical and physical sciences. They give us insight on how systems behave under certain conditions, or how systems evolve as certain state parameters are varied. A chemist observing a reaction in laboratory, or a cosmologist developing a theory for inner star dynamics find great use in applying an equation of state formalism to their respective studies. In general, an equation of state is a three-parameter functional

relating thermodynamic state parameters (such as energy, pressure, temperature, and volume) in a specified environment. There are caloric and volumetric equations of state, and in this thesis, we are interested in the latter, as the unit cell volume of the crystal changes with pressure.

In this thesis, the compression behavior of Fe_3P, synthetic schreibersite, at room temperature was examined using x-ray diffraction methods. By analyzing x-ray diffraction patterns of single crystal Fe_3P, one can determine the unit cell parameters; doing this at various pressures (and given temperature) one can obtain a relation between the unit cell volume and the pressure, i.e. a pressure versus volume isotherm. The following will briefly present some background information on Fe_3P, and on the theory of equations of state used in the present study.

Equations, such as the ideal gas law

$$PV = nRT, \tag{1.1}$$

and Van der Waals' equation of state

$$\left(P + \frac{a}{V_m^2}\right)(V_m - b) = RT, \tag{1.2}$$

are two examples describing how pressure, temperature and volume are related in particular gaseous (and possibly, some liquid) environments [6]. If a state variable (P, V, or T in these cases) were to change, one could infer the equilibrium response of the system by applying such equations of state. It is important to note that any equation of state may break down within the context of extreme conditions i.e. extreme pressures, temperatures, magnetic field, etc. It is up to experiment and theory to ultimately determine the conditions under which the aforementioned equations are valid.

There also exist many equations of state pertaining to the liquid, solid and plasma states of matter. Some notable examples are the Peng-Robinson equation for liquids

(and real gases) [6]

$$P = \frac{RT}{V_m - b} - \frac{a(T)}{V_m(V_m + b) + b(V_m - b)}, \tag{1.3}$$

the 3^{rd} order Birch-Murnaghan equation of state [7]

$$P(V) = \frac{3K_0}{2}\left[\left(\frac{V_0}{V}\right)^{\frac{7}{3}} - \left(\frac{V_0}{V}\right)^{\frac{5}{3}}\right]\left\{1 + \frac{3}{4}(K_0' - 4)\left[\left(\frac{V_0}{V}\right)^{\frac{2}{3}} - 1\right]\right\}, \tag{1.4}$$

and an equation for ideal ion plasmas

$$F_{id} = \sum_j N_j k_B T[ln(n_j \lambda_j^3/g_j) - 1], \tag{1.5}$$

adapted from [8]. In equation 1.5 the F_{id} term represents the free energy of the system, which can in turn be used to calculate thermodynamic state variables of interest , for example

$$P = -\frac{\partial F}{\partial V}. \tag{1.6}$$

Every equation of state is derived based on some physical assumptions. For the case of volumetric equations of state of solids, one can use either the infinitesimal or finite strain theories when discussing the elasticity of the material. Both theories treat the solid as a continuum, but their difference lies in the treatment of derivatives and products of derivatives. We define a strain as infinitesimal when the derivatives of the position vectors relating the initial and strained portions of the volume are small and their squares and products can be disregarded [9, 10]. Conversely, finite strain theory deals with relatively large deformations and the squares and products of the position vector derivatives cannot be neglected.

Based on finite and infinitesimal strain, there are two descriptions used in relating the strained sample and the unstrained sample: these are known as the Eulerian and Lagrangian descriptions respectively. The difference between the two descriptions is

essentially due to the choice of coordinate system to relate the strained and unstrained states of the sample. The Eulerian approach uses the coordinate system of the strained sample, and the Lagrangian approach uses the coordinates of the unstrained sample. In practice, we are usually observing the sample in the strained state, therefore the Eulerian description more naturally suits the problem [10].

The case we are interested in is for a uniformly applied stress throughout the volume of the sample. This is known as a *hydrostatic* pressure environment. Pressure-volume relations derived using *finite strain theory* [10, 7] have provided reliable agreement with experiments under hydrostatic conditions in modest pressure ranges (on the order of several GPa), and will be discussed shortly.

As a first approximation, one can derive of an isothermal equation of state starting from a simple definition of the bulk modulus. At constant temperature, we can relate the bulk modulus to the volume derivative of the pressure, namely

$$K_T = -V \left(\frac{\partial P}{\partial V} \right)_T . \tag{1.7}$$

If we assume that K_T is constant, we find that the density, $\rho = \frac{mass}{volume} \sim e^P$ will go to infinity as the pressure P goes to infinity. Quantum mechanics implies that this result is unphysical for atomic matter, and that K must depend on pressure. Approximating the bulk modulus K to be linearly dependent on pressure we find:

$$K\left(P\right) = K_0 + K_0' P. \tag{1.8}$$

Plugging this into equation 1.7 and integrating each side we find that

$$\frac{m}{V} = \rho = \rho_0 \left[1 + \frac{K_0'}{K_0} P \right]^{\frac{1}{K_0'}} \tag{1.9}$$

where K_0, K_0', and $\rho_0 = \frac{m}{V_0}$ are assumed to be constant. This equation can also be

solved for the pressure as a function of volume, namely

$$P = \left(\frac{K_0}{K_0'}\right)\left[\left(\frac{V_0}{V}\right)^{K_0'} - 1\right]. \tag{1.10}$$

This is known as the *Murnaghan* isothermal equation of state, named after F. D. Murnaghan. This equation is not completely accurate, as the pressure dependencies of K and K' predicted by this model (and models that assume linear pressure dependence on K' as well) do not agree with observations [10]. Experiments tell us that K and K' (as well as higher order derivatives) depend on pressure, and more accurate models are necessary to justify observations [10, 11].

By applying finite strain theory, we can deal with the pressure dependence of K and K' more easily. [10, 7] provides a detailed analysis of finite strain applied to cubic solids, and the above result is readily obtained with appropriate approximations. In practice we find much better agreement with experimental data using higher order corrections. More detailed expressions for the pressure-volume relationship, derived using finite strain considerations, will be presented below; these expressions were compared to the experimental data collected for this thesis project.

A famous result derived in [10] is given by

$$P = a\left(f + 5f^2\right) \tag{1.11}$$

where $a = 3K_0$, $f = \frac{1}{2}\{\left(\frac{V_0}{V}\right)^{2/3} - 1\}$. The f^2 term is a correction to equation 1.10, and we recover 1.10 by ignoring this term. Up to modestly high pressures (several GPa) for various materials, this equation was shown to be fairly reliable. At higher pressures, data tend to disagree with the predictions of the above equation, and more sophisticated models [11, 7] give better agreements.

An isotherm derived by [7] (known as a *Birch-Murnaghan* isotherm) using finite

strain theory applied to a solid under hydrostatic stress is given by

$$P = \frac{1}{2}\left[\left(\frac{V_0}{V}\right)^{7/3} - \left(\frac{V_0}{V}\right)^{5/3}\right]\left[C_2 + \frac{D_3}{2} - \left(\frac{D_3}{2}\right)\left(\frac{V_0}{V}\right)^{2/3} + \cdots\right] \tag{1.12}$$

where C_2 and D_3 are constants relating to the bulk modulus and its pressure derivative. This relation agrees well with experiments up to relatively high pressures, and is more accurate than the expression in equation 1.11

Additionally a *universal* or *Vinet* equation of state for solids was proposed by [11] using energy considerations of inter-atomic separation distances, and (at constant temperature) is of the form

$$P(x) = 3K_0(1-x)x^{-2}\exp\left[\frac{3}{2}(K_0' - 1)(1-x)\right] \tag{1.13}$$

where $x = (V/V_0)^{1/3}$. This equation gives the best agreement over a wide array of materials and up to higher pressures, as this model more accurately represents the physical world. The exponential dependence in the Vinet equation reflects characteristic interatomic repulsions, whereas the B-M is based on continuum mechanics, which is not completely physical for the case of crystals. The B-M equation is also limited by the fact that it is a truncated Taylor series, thus the predictions are incomplete. We choose to use a Vinet isotherm for the fitting of data collected in this experiment and compare with the predictions of the 3^{rd} order Birch-Murnaghan equation of state given by equation 1.4.

This introduction serves to inform one of equations of state and how scientists may apply them to various situations. For this case, we want an equation of state evaluated at room temperature (an isotherm). Using the results derived by [10, 7, 11], we attempt fit the experimentally obtained compression data of Fe_3P. X-ray diffraction techniques were employed for determining the unit dimensions, therefore the unit cell volume V, of Fe_3P at various pressures. The following chapter will present some essential theoretical framework regarding crystallography, elastic x-ray scattering and

diffraction. The experimental chapter will present and discuss the physical tools used perform the experiment, and the analysis and results chapter will present the data with applications of theoretical models developed within the document. The discussion and conclusions chapter will emphasize the significance of the results found in this thesis in addition to results found from independent researchers.

CHAPTER 2

THEORETICAL BACKGROUND

Presented in this chapter are some fundamental theoretical considerations relevant to crystal structures and x-ray diffraction studies. These include crystal symmetries, Miller indices, the Bragg and Laue conditions, basics of x-ray scattering theory, among several other important aspects relevant to the thesis topic.

2.1 Crystals and Symmetry

The study of the atomic/molecular ordering of matter is known as *crystallography*. Modern crystallographic techniques, namely x-ray, neutron, and electron diffraction, are used mainly for structure determination, electron density distributions, and atomic positioning. Some common applications include structure determination/confirmation, inspecting a material for defects, and observing the evolution of the structure in a changing local environment.

In crystalline materials, constituent atoms are periodically arranged within the volume i.e. each atom in the crystal is positioned at a fixed distanced relative to each of its nearest neighbors. In contrast to crystals are amorphous materials where there is no periodic connection between the constituent atoms/molecules (e.g. window glass and polystyrene are considered amorphous). In reality there are two types of crystals: monocrystals (known as *single* crystals) and polycrystals. A single crystal is a material whose entire sample volume has a periodic atomic arrangement, whereas a polycrystal's volume consists of many juxtaposed single crystals. In polycrystals, the domains of single crystallinity are called *crystallites* and the boundaries between these regions are called *grain boundaries*. Generally, real single crystals have defects/irregularities which cause deviations from the strict definition of a single crystal. In practice, defects can usually be accounted for and in some cases are desired.

Real single crystals found in nature can be anywhere from nanometers to meters in length, although relatively large crystals are quite rare. It is also possible to "grow" crystals in the laboratory under sufficiently careful conditions. There are also liquid crystals (flow like liquid, but molecules are ordered) and are found both in nature (e.g. various proteins and enzymes) and technology (e.g. modern electronic display screens). Figure 2.1 depicts a crystallographic reference system for atomic positions in a crystal.

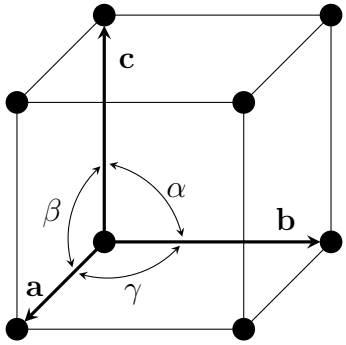

FIGURE 2.1: A parallelepiped generated by the vectors **a**, **b**, and **c**. In some cases, **a**, **b**, and **c** may be orthogonal ($\alpha = \beta = \gamma = \frac{\pi}{2}$), but it is not a requirement. The parallelepiped represents the *unit cell* of a crystal, each unit cell being a building block of the crystal lattice; the black circles represent the constituent atoms. The magnitudes of vectors **a**, **b**, and **c** (a,b, and c) along with the angles α, β, and γ are known as the *unit cell parameters*.

The vectors **a**, **b**, and **c** define the unit cell of the system; a linear combination of the unit cell vectors, namely $\mathbf{r} = n_1\mathbf{a} + n_2\mathbf{b} + n_3\mathbf{c}$ where n_1, n_2, and n_3 are integers, describe a corner position of a unit cell in the crystal. The unit cell parameters (see figure 2.3) , namely a, b, c, α, β, and γ, define the shape of each unit cell in the given crystal. The function **r** described above can be used to generate a lattice spanned by the unit cell vectors. Figure 2.2 shows a simple lattice consisting of eight unit cells, with atoms at the corners of each unit cell.

Some lattices contain atoms at fractional multiples of the unit cell distances. For example, a lattice may contain atoms at $r = (\frac{m_1 a}{2}, \frac{m_2 b}{2}, \frac{m_3 c}{2})$, where m_1, m_2 and m_3 are

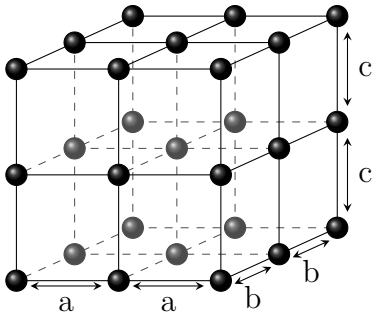

FIGURE 2.2: Depicted above is a lattice generated from 8 unit cells. Note how contingent unit cells share atoms: 27 atoms comprising 8 unit cells in this case.

integers, in addition to the atoms at $r = (n_1a, n_2b, n_3c)$. There are other possibilities as well, a total of 14 possible crystalline lattice types. This was first shown by the French scientist Auguste Bravais in 1850 [12]; these are known as the *Bravais* lattices. Each lattice belongs to one of the 7 *crystal systems* with a particular lattice centering. Figure 2.3 shows the 7 crystal systems and 14 Bravais lattices.

The local atomic layout in any single crystal can be characterized by one of the fourteen Bravais lattices. In addition to Bravais lattices, a crystal's symmetry is further characterized by its *point group* or *crystal class*. The point group is a mathematical group of operations (known as *symmetry operations*) that may be performed on the lattice that leave it unchanged. There are four types of symmetry operations that pertain to point groups, namely reflection, inversion, rotation, and improper rotation (this is a reflection following a rotation). The reflection operation is performed with respect to a specific plane, and the improper rotation reflection plane is perpendicular to the rotation axis. The term "point group" is used because the operations are performed relative to a point (or set of points) in the lattice (e.g. an inversion about a point, or a rotation axis containing multiple points). There are a total of 32 point groups in all.

In addition to the 32 point groups, by including the translational symmetry operation one can derive the 230 *space groups*. Symmetry operations such as ordinary

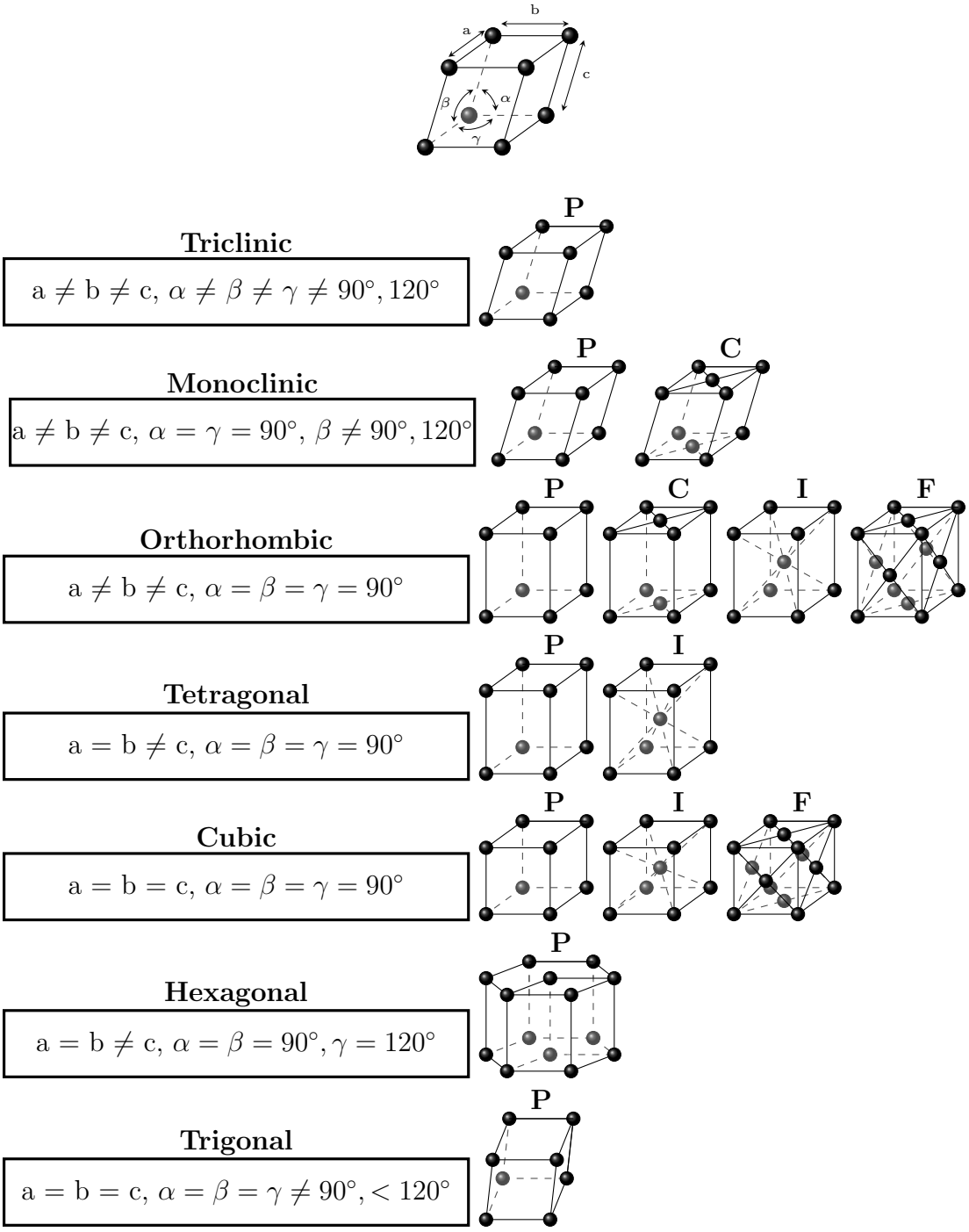

FIGURE 2.3: The 14 possible Bravais lattices among 7 crystal systems. Lattice centerings: P-primitive, I-body-centered, F-face-centered, C-base-centered, R-rhombohedral. Note some unit cells have atoms at fractional unit cell distances

translations, a translation followed by a rotation (known as a *screw axis*), and a translation followed by a reflection (known as a *glide plane*) are included within a space group. It is common in the field of crystallography to refer to a material by its space group as this contains all the necessary information regarding the long range atomic symmetry in the sample. [12] gives a detailed overview of point groups and space groups.

As mentioned above, once a space group for a material is established, one can predict the long range order of the sample. In cases where the crystals are sufficiently large, one can determine many of the symmetry elements by visual inspection. By defining a reference system, one can check for various symmetry operations by rotating the crystal and also by imagining an inversion operation about a point, or a reflection about a plane. Crystals that are relatively small would need to be analyzed with a reflection goniometer with an attached monocular, if plausible.

In addition to visual inspection, one can get a much more complete understanding of a crystalline species using x-ray diffraction methods, as we are probing the sample at the atomic level. We can observe and record the physical properties of many types of crystals without extensive knowledge of the atomic makeup of the crystal. X-ray diffraction allows us to analyze and determine the structure of a sample (atomic distribution), which allows us to justify and predict observable macroscopic effects. More on this will be discussed in following sections.

2.2 Reciprocal Lattice and Miller Indices

The reciprocal lattice is a mathematical construct useful in describing *atomic* or *crystal planes* in crystals. Each point in the reciprocal lattice corresponds to a family of real parallel planes, each equally spaced with respect to neighboring planes. In practice, a crystal plane represents a two-dimensional net of atoms, all lying in the same plane. The distance between planes, known as the *d-spacing* may be found

from the definitions of the reciprocal lattice, expressed in terms of the real lattice. Therefore if we have an accurate representation of the reciprocal lattice we can, within experimental error margins, determine the real lattice dimensions. The x-ray diffraction section will discuss some of the practical applications of the reciprocal lattice.

The spatial periodicity of a lattice can be defined mathematically by the relation

$$R(\mathbf{x}) = R(\mathbf{x} + n_1\mathbf{a} + n_2\mathbf{b} + n_3\mathbf{c}) \tag{2.1}$$

where n_1, n_2, and n_3 are integers and **a, b**, and **c** are the unit cell vectors of the real lattice. By expanding the function R as a Fourier series, we may represent it as

$$R = \sum_{\mathbf{h}} R_{\mathbf{h}} e^{i\mathbf{l}\cdot\mathbf{x}}. \tag{2.2}$$

The periodicity of the lattice requires that $R(\mathbf{x}) = R(\mathbf{x} + \mathbf{r})$, where $\mathbf{r} = n_1\mathbf{a} + n_2\mathbf{b} + n_3\mathbf{c}$. This means that the exponential factors of the function R must remain the same if $\mathbf{x}$ is replaced by $\mathbf{x} + \mathbf{r}$, leading to the fact that $\mathbf{r} \cdot \mathbf{h} = m2\pi$. Writing $\mathbf{r}$ explicitly in component form, we find that $\mathbf{a} \cdot \mathbf{h} = 2\pi h_1, \mathbf{b} \cdot \mathbf{h} = 2\pi h_2, \mathbf{c} \cdot \mathbf{h} = 2\pi h_3$, where h_1, h_2 and h_3 are positive or negative integers or zero. The solution of these three equations is

$$\mathbf{h} = h_1\mathbf{l_1} + h_2\mathbf{l_2} + h_3\mathbf{l_3}. \tag{2.3}$$

The $\mathbf{l}_i$ vectors, which are reciprocal unit cell vectors that span the reciprocal space in question, can be expressed in terms of the unit cell vectors, namely

$$\mathbf{l_1} = \frac{2\pi\mathbf{b}\times\mathbf{c}}{\mathbf{a}\cdot\mathbf{b}\times\mathbf{c}} \equiv \mathbf{a}^\star, \mathbf{l_2} = \frac{2\pi\mathbf{c}\times\mathbf{a}}{\mathbf{a}\cdot\mathbf{b}\times\mathbf{c}} \equiv \mathbf{b}^\star, \mathbf{l_3} = \frac{2\pi\mathbf{a}\times\mathbf{b}}{\mathbf{a}\cdot\mathbf{b}\times\mathbf{c}} \equiv \mathbf{c}^\star. \tag{2.4}$$

As was mentioned in the beginning of the section, each point in the reciprocal lattice represents a family of planes, each plane being separated by a constant distance. This can be visualized by the equation

$$\mathbf{h} \cdot \mathbf{r} = 2\pi m = 2\pi \left(n_1 h_1 + n_2 h_2 + n_3 h_3 \right) \tag{2.5}$$

where m is some given constant. As was stated before, the various n_i and h_i must be integers, therefore the constant m must also be an integer. 2.5 represents a plane (known as a *crystal plane*) containing an infinite number of Bravais lattice points, and the n_i satisfying 2.5 for each given set of h_i require that an infinite number of planes be generated for the various integer values of the constant m. Therefore one can conclude that for a given set of h_i integers one can define an infinity of planes all parallel and equally spaced apart, assuming an infinite real lattice to begin with.

The integers h_1, h_2 and h_3 are known as the *Miller indices* and are of great practical importance in crystallographic studies. In practice it is convenient to impose the constraint that the Miller indices are mutually prime; this is done so there are not an infinite number of sets of Miller indices describing the same family of planes. One can relate the adjacent crystal plane separation, or *d-spacing*, from the Miller indices and unit cell parameters [reference]. Each crystal system has a unique equation relating the d-spacing to the Miller indices and unit cell parameters, cubic being the simplest, triclinic being the most complex.

To derive the spacings between crystal planes, we first start with the distance from an origin to a crystal plane, or $\frac{2\pi m}{h}$, and the adjacent plane $\frac{2\pi(m+1)}{h}$, and take the difference, leaving $d = \frac{2\pi}{h}$ [13].$\mathbf{h}$ is the vector from the origin to a point in reciprocal space, labelled $\mathbf{h}(h_1, h_2, h_3) = h_1\mathbf{a}^\star + h_2\mathbf{b}^\star + h_3\mathbf{c}^\star$. Starting with the definition of $\mathbf{h}$ we have

$$\mathbf{h} \cdot \mathbf{h} = (h_1\mathbf{a}^\star + h_2\mathbf{b}^\star + h_3\mathbf{c}^\star) \cdot (h_1\mathbf{a}^\star + h_2\mathbf{b}^\star + h_3\mathbf{c}^\star) \tag{2.6}$$

$$\begin{aligned}\mathbf{h}^2 = h_1^2\mathbf{a}^\star\cdot\mathbf{a}^\star + h_1h_2\mathbf{a}^\star\cdot\mathbf{b}^\star + h_1h_3\mathbf{a}^\star\cdot\mathbf{c}^\star \\ + h_2h_1\mathbf{b}^\star\cdot\mathbf{a}^\star + h_2^2\mathbf{b}^\star\cdot\mathbf{b}^\star + h_2h_3\mathbf{b}^\star\cdot\mathbf{c}^\star \\ + h_3h_1\mathbf{c}^\star\cdot\mathbf{a}^\star + h_3h_2\mathbf{c}^\star\cdot\mathbf{b}^\star + h_3^2\mathbf{c}^\star\cdot\mathbf{c}^\star\end{aligned} \tag{2.7}$$

$$\begin{aligned}\mathbf{h}^2 = h_1^2a^{\star 2} + h_2^2b^{\star 2} + h_3^2c^{\star 2} + 2h_2h_3b^\star c^\star\cos\alpha^\star \\ + 2h_3h_1c^\star a^\star\cos\beta^\star + 2h_1h_2a^\star b^\star\cos\gamma^\star.\end{aligned} \tag{2.8}$$

We can put this in terms of real lattice parameters using the transformations given in equations 2.4 and the figure 2.1. Doing this we find that

$$\begin{aligned}a^\star &= 2\pi bc(\sin\alpha)/V_r \\ b^\star &= 2\pi ac(\sin\beta)/V_r \\ c^\star &= 2\pi ab(\sin\gamma)/V_r \\ \cos\alpha^\star &= (\cos\beta\cos\gamma - \cos\alpha)\,/\,(\sin\beta\sin\gamma) \\ \cos\beta^\star &= (\cos\alpha\cos\gamma - \cos\beta)\,/\,(\sin\alpha\sin\gamma) \\ \cos\gamma^\star &= (\cos\beta\cos\alpha - \cos\gamma)\,/\,(\sin\beta\sin\alpha)\end{aligned} \tag{2.9}$$

where $V_r = \mathbf{a}\cdot\mathbf{b}\times\mathbf{c} = abc\,(1-\cos^2\alpha-\cos^2\beta-\cos^2\gamma+2\cos\alpha\cos\beta\cos\gamma)^{1/2}$.We can plug these into $\mathbf{h}^2$, then take the square root of $\mathbf{h}^2$, and plug this into the equation $d = \frac{2\pi}{h}$ to find the spacing between parallel crystal planes belonging to the same family. We label this spacing as $d(h_1, h_2, h_3)$. The most general case is the triclinic case, where $a \neq b \neq c$ and $\alpha \neq \beta \neq \gamma$, and the expression for $d(h_1, h_2, h_3)$ is quite complex. For simpler cases where there is greater symmetry, the expression for $d(h_1, h_2, h_3)$ may be greatly simplified.

For the sample under investigation, the crystal symmetry is tetragonal. This

means that $\alpha = \beta = \gamma = 90^0$ and $a = b$, and we find that

$$d(h_1, h_2, h_3) = \frac{V_r}{(h_1^2 a^2 c^2 + h_2^2 a^2 c^2 + h_3^2 a^4)^{1/2}} = \frac{a^2 c}{(h_1^2 a^2 c^2 + h_2^2 a^2 c^2 + h_3^2 a^4)^{1/2}} \quad (2.10)$$

rewriting this in a more convenient and traditional form, namely $1/d^2$, we find

$$\frac{1}{d^2} = \frac{h_1^2 + h_2^2}{a^2} + \frac{h_3^2}{c^2} \quad (2.11)$$

for a crystal with tetragonal symmetry.

Applications of Miller indices and reciprocal space to the thesis topic will be elucidated further in several of the following sections and chapters. The experimental chapter will include how equation 2.11 directly applies to the determination of the unit cell parameters from the experimental data.

2.3 X-ray Scattering and Diffraction

The phenomena of scattering and diffraction is well founded and may be applied in any range of the electromagnetic spectrum. For the case of crystals, the scatterers are electrons bound to atoms fixed in a lattice and periodically spaced throughout the volume. The periodicity of the atomic layout makes crystal structures ideal diffraction gratings for electromagnetic radiation in the x-ray region. This section will present an overview of the x-ray scattering process and discuss how diffraction can yield pertinent information regarding the state of a crystal.

In classical physics, diffraction refers to the modulation of waves subsequent to interaction with matter. Diffraction occurs for every type of wave, and electromagnetic radiation may be described in terms of waves. The diffraction features are prominent when the wavelength of the wave is on the order of diffracting obstacle; effects are more apparent in a given wavelength range for any given obstacle or set of obstacles.

For optical radiation ($400nm \lesssim \lambda \lesssim 700nm$), diffraction effects may be pronounced using a diffraction grating where the diffracting objects are on the order

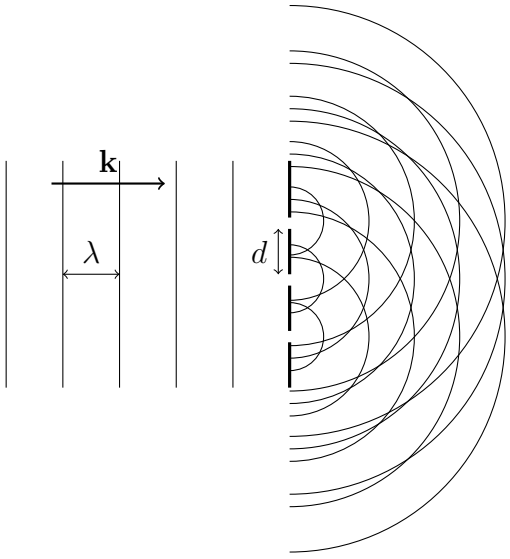

FIGURE 2.4: Plane waves incident on a diffraction grating with spacing d. Areas of overlap of spherical wavelets signify constructive interference, where open areas signify destructive interference

of micrometers and regularly spaced apart. A diffraction grating may be used to exploit the superposition of waves to obtain regions of constructive and destructive interference. Figure **??** depicts the effects of collimated monochromatic plane waves of wavelength λ impinging on a diffraction grating with some spacing d.

diagram allows one to derive a relationship between d, λ and θ for constructive and destructive interference. One finds that the light waves will constructively interfere for

$$n\lambda = dsin\theta \tag{2.12}$$

where $d \sin\theta$ is the optical path length difference between rays from adjacent slits, and n is an integer. It is also assumed in this case that the incident angle between the plane waves and grating normal is zero. Therefore if we know any of the two of d, λ or θ, we can determine the third. In practice this can be verified by placing a screen or film some distance from the grating and recording the interference pattern.

At photon energies used in this experiment, the dominant interaction between the

photons and matter (electrons) is Compton scattering [14], where the energy of the scattered photon is given by

$$E' = \frac{E}{1 + (E/mc^2)(1 - \cos\theta)}. \tag{2.13}$$

. For the scatters in a crystal, most electrons are tightly bound to the nucleus, and the recoiling system is the entire atom. The mass in the above equation will be on the order of the mass of the atom, yielding and unmeasurable shift in energy between incident and scattered photons for essentially all measurable angles. Larger shifts in wavelength could be observed for bonding electrons, as they less constricted by the nucleus. In high Z solids, almost all electrons are tightly bound and the Compton shift is unobservable at these energies. The interaction cross section for Compton scattering dominates in the region where $0.1 \lesssim \frac{h\nu}{mc^2} \lesssim 1$, and for this experiment we have $\frac{h\nu}{mc^2} \sim 0.1$, for which we have $\sigma_C \sim \sigma_T$, where σ_T is the *Thomson* scattering cross-section. Thomson scattering (or elastic scattering of x-rays) agrees with observations in this energy regime, and is therefore a reliable model in x-ray diffraction. Treating the scattering process as elastic is key in developing some useful models in x-ray diffraction.

In x-ray diffraction, we can take an analogous approach to derive a relationship between x-ray wavelength and crystal plane spacing. Since the scattering of x-rays will be elastic in this case, we treat the crystal lattice as a three-dimensional diffraction grating, where the scatterers are periodically arranged in space. A crystal plane is an imaginary plane containing regularly spaced atoms; each plane repeats itself a distance d normal to the face of the plane (the d-spacing). Each atom can be thought of as a positively charged nucleus surrounded by a negatively charged cloud of electrons. We assume that electromagnetic waves are incident on the electron cloud, the electron cloud distorts and the moving electrons causes a re-radiation of the waves in all directions, assuming unpolarized incident radiation. This is known

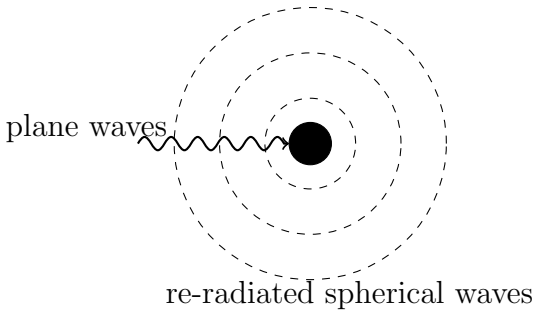

FIGURE 2.5: Simplistic diagram of plane waves $\vec{E} = E_0\hat{x}\cos\omega t$ incident on an atomic electron cloud and re-radiated. This process is elastic, meaning the re-radiated waves are of the same wavelength as the incident radiation.

as *Rayleigh* or *Thomson* scattering and is shown schematically in Figure 2.3. This model works well in practice, but it ignores the true quantum effects governing the process.

If unpolarized x-radiation is incident upon an array of atoms, we get scattering from each atom in all directions. Where the waves overlap, we get reinforcement of the waves; destructive interference occurs in other regions. A ray diagram is a useful representation of this process (see 2.3). Incident plane waves are represented as rays perpendicular to the wave fronts, parallel to the propagation direction. Incident rays interact with the atoms in a crystal plane and "reflect" in some direction. Assuming the law of reflection holds, the incident angle is the same as the reflection angle. There is no relative phase difference between scattered waves of the same crystal plane. The rays interact with atoms in an adjacent crystal plane a short time later, and therefore differ in phase by some amount. When the phase difference is some multiple of 2π, constructive interference occurs. This is equivalent to a ray path difference of $n\lambda$, where n is an integer and λ is the wavelength. Again, by invoking that the path length difference between rays reflecting from adjacent planes must equal an integer multiple of wavelengths, we arrive at the result

$$n\lambda = 2dsin\theta. \tag{2.14}$$

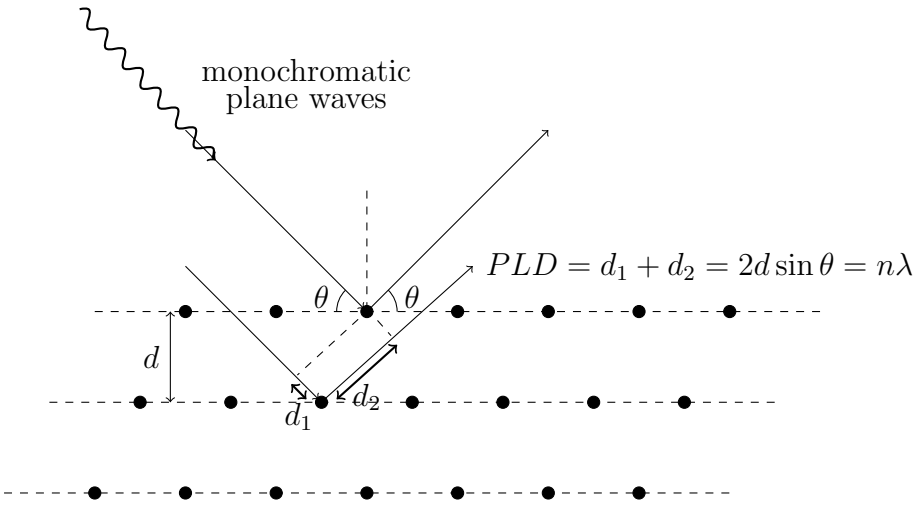

FIGURE 2.6: Two dimensional representation of monochromatic plane waves incident on atoms in a crystal. Black dots represent atoms, dashed lines represent crystal planes, and d is the spacing between adjacent parallel planes. The difference in ray paths is known as the *path length difference* (PLD); constructive interference occurs for $PLD = n\lambda$.

This model is known as *Bragg's law* and works very well for various practical applications in x-ray diffraction. With a monochromatic x-ray source and a given crystalline sample, we can observe constructive interference at angles where the Bragg condition is met.

In addition to Bragg's law is the *Laue* treatment of x-ray diffraction. In this model rays are imagined to be scattered, or redirected by the atoms. The scattered rays will constructively interfere for path length differences of multiples of 2π. This is best visualized by the one-dimensional sketch shown in figure 2.3. The path difference $AC - BD$ can be expressed in terms of the angles ϕ and ψ, namely

$$AC - BD = a\left(\cos\psi - \cos\phi\right). \tag{2.15}$$

When the path difference equals an integer number of wavelengths, constructive interference occurs, or

$$h\lambda = a\left(\cos\psi - \cos\phi\right). \tag{2.16}$$

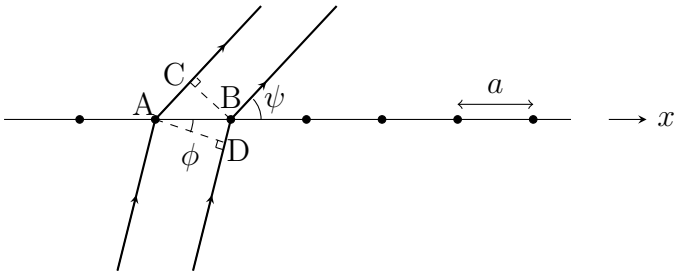

FIGURE 2.7: X-rays incident on a one-dimensional row of scatterers (black dots) separated a distance a . Constructive interference occurs when the ray path difference $AC - BD$ is an integer multiple of the wavelength λ.

For a given incident angle ϕ, there can be multiple orders of diffraction, as h and ψ can change (h is an integer, ψ is continuous) while the interference condition is also satisfied. Also, equation 2.16 does not require that the x-rays be scattered in the plane of the incident radiation; the scattering angle ψ is with respect to the coordinate axis x, and a cone of scattered x-rays can be imagined. We therefore can envision multiple cones, each with a different angle ψ defining them.

We can generalize this to a net (two-dimensional array) of scatterers to obtain two interference condition equations, namely

$$h\lambda = a\left(\cos\psi_1 - \cos\phi_1\right) \tag{2.17}$$

$$k\lambda = b\left(\cos\psi_2 - \cos\phi_2\right).$$

When one of the equations is satisfied, we arrive at the results for the one-dimensional case. When both equations are satisfied, the net is said to scatter in phase and constructive interference occurs along the lines of intersection of the cones of angles ψ_1 and ψ_2. Further generalizing to a three-dimensional array we obtain the *Laue*

equations, given by

$$h\lambda = a\left(\cos\psi_1 - \cos\phi_1\right) \tag{2.18}$$

$$k\lambda = b\left(\cos\psi_2 - \cos\phi_2\right)$$

$$l\lambda = c\left(\cos\psi_3 - \cos\phi_3\right).$$

If any of the above three equations is satisfied, enhancement of the x-rays at the specified angles can be observed. If all three of the above equations are satisfied, the entire three-dimensional array scatters in phase (each of the cones described by their respective angles intersect in a line). The integers h, k, and l are synonymous with the Miller indices described in section 2.2, and a, b, and c are the unit cell lengths. This model also works well for x-ray diffraction studies, and can be shown to be equivalent to the Bragg treatment of x-ray diffraction. Depending on the situation, the use of one model over the other may be more convenient to apply, and this will be discussed in the experimental chapter.

CHAPTER 3

EXPERIMENTAL

The majority of modern high pressure experiments employ the use of diamond anvil cells, large volume presses, and shock waves to generate high pressures. Probing the samples under these conditions requires the use of conventional measuring instruments, such as diffractometers and spectrometers, but modified to accommodate the obstructing pressure generating apparatuses. This chapter will describe and present the methods and devices used to perform these experiments in particular.

3.1 Diamond Anvil Cell: Concepts and Components

The diamond anvil cell (DAC) is a primary device used in modern static high pressure experiments of microscopic samples. With this device, one can generate pressures on the order of $\sim$ 3 Mbar [15]. The main components of a traditional DAC are a metallic cell body, diamonds, diamond backing plates (or diamond *seats*), screws, and washers (see figure 3.1). Depending on the type of DAC, there may be additional/substitutional components to suit experimental needs, such as lever arms and pressure driven membranes.

The DAC is based on the concept of opposing rigid anvils drawn closer to squeeze a small volume. The basic principle of the DAC is to apply a large force to a small area and thus generate a high pressure. In some cases, it is desired to have non-uniform stress and strain applied to the sample. In most cases, and in the case of this thesis, one would like to create an environment where the stress is uniform over the sample volume (hydrostatic pressure).

To apply a large uniform pressure to a sample, we create a *sample chamber* by placing a holed metal gasket between the diamonds. The chamber is the volume bounded by the gasket and the diamond tips. The sample chamber contains the sample, a *pressure medium*, and a *pressure marker*. The pressure medium, which

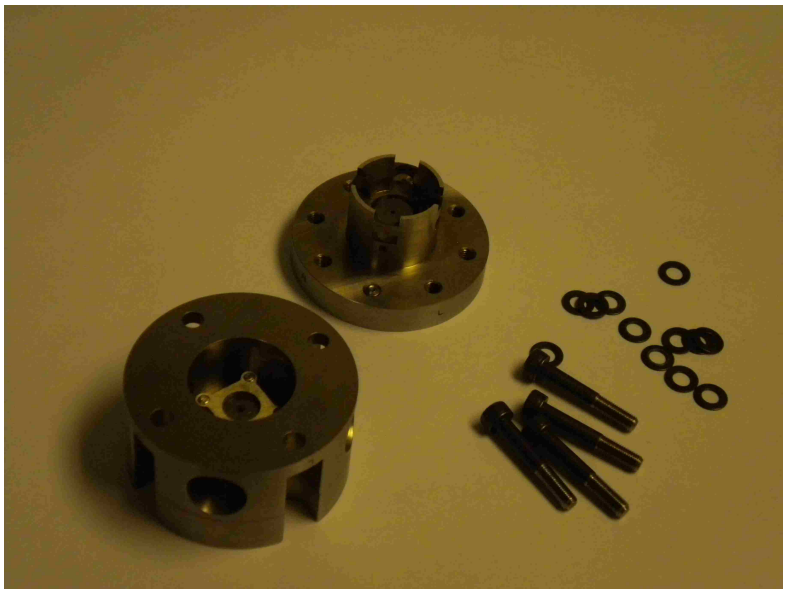

FIGURE 3.1: A picture showing a typical diamond anvil cell. The screws bring the diamonds closer causing a larger force, therefore pressure, on the sample environment.

is generally a gas or liquid at room temperature, fills the sample chamber. When pressure is applied, the pressure medium (ideally) uniformly transmits the pressure throughout the volume of the sample chamber. The pressure marker is something the scientist uses to indirectly measure the pressure within the chamber. More on pressure media and markers will be discussed shortly. Figure 3.1 shows a simple schematic of this concept.

In order to have a successful experiment, the DAC must be properly prepared. This begins with correctly mounting diamonds on a diamond seat. The hole of the diamond seat should be centered about the diamond axis. The importance of diamond centering becomes greater as the desired pressures become greater, although care should be taken even for relatively low pressure ranges. There are several different methods for doing this, and for this experiment a *jig* (see 3.1) and epoxy glue were used. The jig is a device used for centering the diamonds on the seat while holding them still. Once the diamonds are secured, one can shift the position of the seats using the set screws on the outside to center the seat hole about the *diamond axis*;

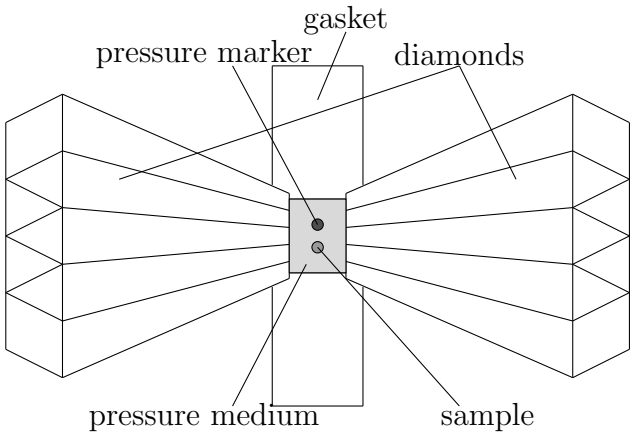

FIGURE 3.2: A cross-sectional schematic showing the fundamental concept of the diamond anvil cell. Two opposing diamonds and a gasket form a sample chamber containing the pressure medium, pressure marker and sample. As the diamonds are drawn closer together, the sample chamber is condensed and the pressure inside the chamber increases. The pressure within the chamber is estimated indirectly with the aid of the pressure marker.

FIGURE 3.3: A picture of two jigs, one open and one closed. This device presses the bottom face of the diamond against the diamond seat while allowing the seat to be translated until the seat axis and diamond axis coincide. The openings on the perimeter allow one to apply glue where the diamond meets the seat.

the diamond axis coincides with the line perpendicular to the culet plane and passing through its center. A microscope is used for this process as the diamond culets are on the order of hundreds of micrometers in diameter. Once the diamond is correctly centered and held in place, epoxy glue is applied along boundary of the seat/diamond interface. To expedite the curing process, the jig can be placed in an oven for some predetermined time (this depends on temperature and the type of epoxy).

Next, they are placed in the DAC and secured with screws. After locking the diamond seats in place, one must ensure that the diamond culets are parallel and aligned. This is also done under the microscope. The DAC is put together and the diamond culets are then brought very close together ($< 1mm$). The screws that hold the seats in place are used to translate the seats such that the opposing diamonds can aligned along the same axis. Looking down the diamond axis under the microscope one can adjust the set screws of one seat to bring both diamonds into alignment. One can observe how parallel they are from a side view under the microscope. If the diamond cell is built correctly, the diamond culets should be parallel once the seat screws are tightened (some cells are built with a rotational stage underneath one of the seats, allowing the diamond's axis to be translated and rotated). If the diamonds are not parallel, one should observe white light (from the microscope) interference fringes when looking through the microscope, focused on the culet faces. The diamond culets and the air between them form an etalon. When they are significantly unparallel, the constructive interference condition is simultaneously satisfied for all wavelengths in the continuous band of optical light (from the microscope lights) over many orders. The quality of the experiment, for various reasons, require that the diamonds be sufficiently parallel (zero to a couple of interference fringes). Unparallel diamonds cause non-uniform gasket thickness, asymmetric gasket deformation, possible diamond failure, among other undesired effects.

Once the diamonds are properly mounted and the seats are positioned correctly, a gasket must be prepared. The gasket is a small (mm^2), thin ($200\mu m$) metal disc or rectangle that is indented, drilled, and placed between the diamonds. Some of the most common gaskets are made of steel, rhenium, and beryllium.

First a potential gasket is chosen and the initial thickness is measured. Typically this is around $\sim 200\mu m$. Then, it is centered between the diamonds, with no applied pressure other than gravity. Next, one can measure the distance between the top and bottom of the diamond cell (this will act as a reference position to gauge how much the gasket has been compressed). A particular washer arrangement should also be chosen prior to indenting. The washers around the diamond cell screws are known as *Belleville* washers, and are designed to recoil and store energy as they are compressed. They are cupped (with some radius) and behave similar to springs when compressed parallel to the washer axis. The arrangement of washers on an individual screw acts similar to springs in series, and collectively they act as springs in parallel. The stiffness of each of the "springs" can be varied by choice of washer and by adjusting the washer arrangement (see figure 3.4).

Then, one can slowly turn the screws in the DAC and slowly indent the metal gasket. This will cause the diamonds to press into the metal, decreasing the thickness of the metal between the diamonds. Measuring the top to bottom DAC distance after each round of turns (after turning each screw the same amount) can give a reasonable estimate of how much the gasket has been compressed. By taking the difference between the initial gasket thickness and the amount of change in top to bottom DAC distance, we get the approximate thickness of the gasket, which is the distance between the diamond culets.

The thickness and type of gasket must be considered prior to experiment. The thickness must be smaller for higher pressure experiments. As the pressure increases, the walls of the sample chamber will continue to shrink. If the gasket is too thick the

walls will close in (sample chamber collapse) before the desired pressure is reached. The type of gasket should also be considered, as some situations are better suited for specific gaskets. A gasket may be shaped in a disc or rectangle, and is usually made of some metal or alloy. A soft low Z material such as beryllium is good for low energy x-ray experiments, as there is very little absorption or scattering from this material. Also, softer gaskets, such as stainless steel and beryllium, are reliable over modest high pressure ranges. At higher pressures, a hard material such as rhenium must be used to avoid collapse of the sample chamber.

Once the desired thickness is reached, one can relieve the stress on the gasket by slowly unscrewing the screws. This leaves the gasket with diamond impressions on either side. The perpendicular distance between culet impressions is the gasket thickness, and can be measured with a micrometer. For harder materials (such as rhenium), one must indent slightly passed the desired thickness, due to elastic recoil.

Next, a hole in the gasket must be drilled to make a sample chamber (sample chamber bounded by gasket hole and diamond culets. An *electric discharge machine* (see figure 3.1) is a tool that allows for the microscopic drilling of metals. This machine is designed to apply an electrical discharge between electrodes submerged in a dielectric liquid. One electrode is the drill bit face (the drill bit is a cylinder on the order of hundreds of micrometers in diameter) and the other the metal gasket. The electric discharge slowly erodes a circular portion of the metal gasket in the center of the indentation. Over time, a hole is "drilled" out cylindrical hole in the gasket. A voltmeter is used to indicate when this process is complete (a large change in voltage tells us that a hole has been made).

After the drilling is complete, the diamond culets must be cleaned (residual gasket metal may interfere with the experiment) and the diamond cell can be loaded. The drilled gasket placed on one diamond (in the same orientation as in the indentation process) and fastened using putty or quick dry glue. One may then place the sample

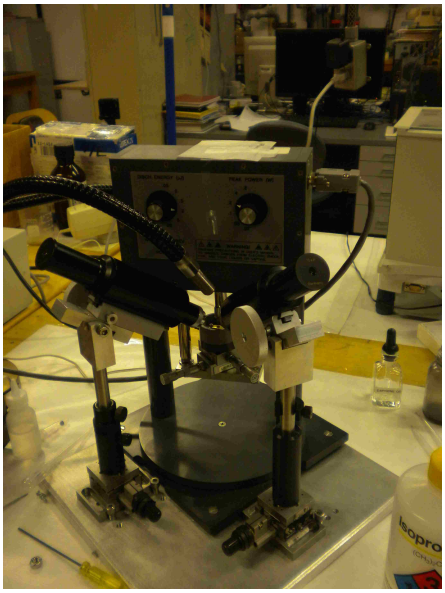

FIGURE 3.4: A picture showing the electric discharge machine apparatus.

and pressure marker within the hole of the gasket (the sample chamber). A pressure medium is inserted into the sample chamber, and the chamber is then sealed off by bringing the opposing diamond into firm contact with the gasket. The pressure inside the sample chamber will differ based on how tightly the screws are tightened; they must be tight enough to ensure pressure medium does not leak.

3.2 Pressure Media and Markers

The pressure medium is a substance used to transmit the pressure applied by the diamonds to the sample chamber (thus the sample). This substance in general is a liquid or gas at room temperature; once high pressures are reached the medium freezes, and hydrostaticity is lost. Though these substances will eventually solidify under pressure, some, such as the inert gases, remain rather soft and conditions are close to hydrostatic up to high pressures. Some, on the other hand, become very hard at certain pressures sustaining large pressure gradients within the sample chamber, and a hydrostatic environment is no longer a valid approximation.

The most reliable (for quasi-hydrostatic conditions) pressure media for high

pressure research are the inert gases, such as neon, argon, and helium [16]. One key benefit is that there will be no chemical reaction between sample and medium. Also, though these substances solidify, they are soft and yield quasi-hydrostatic conditions up to fairly high pressures, helium being the softest over the largest range.

Cryogenic liquids, such as liquid nitrogen or argon, are also used as they are also highly non-reactive substances. These materials are also fairly soft up to modest pressure ranges.

Silicon oil and a 4:1 methanol:ethanol ratio provide quasi-hydrostatic conditions over smaller pressure ranges ($\sim 10GPa$), but are much more accessible and easier to handle and load. The chances of flushing the sample and pressure marker out of the sample chamber during the loading process are much smaller for these pressure media, as gas and cryogenic loading pose some formidable challenges. In the case of methanol/ethanol, it is common practice that one use a 4:1 ratio as this will maintain the hydrostatic condition in the sample chamber from 7 to $10GPa$ [17]. One may also add water to this solution (ratio 16:3:1 methanol:ethanol:water) for hydrostaticity up to slightly higher pressures (the methanol/ethanol pressure medium is hydrostatic to roughly 10 GPa [17]).

In addition to pressure media, an adequate pressure marking procedure must be implemented. Modern diamond anvil cell experiments commonly use the wavelength shift of the $R1$ ruby fluorescence line [18], as well as equations of state for well known materials, such as gold and platinum [19], to indirectly determine pressure. [19] gives a recent account of the equations of state for six metals (including gold and platinum), as well as a proposed re-calibration for the ruby scale. The pressure for data presented in this thesis was estimated using both the ruby fluorescence technique and the equation of state for gold.

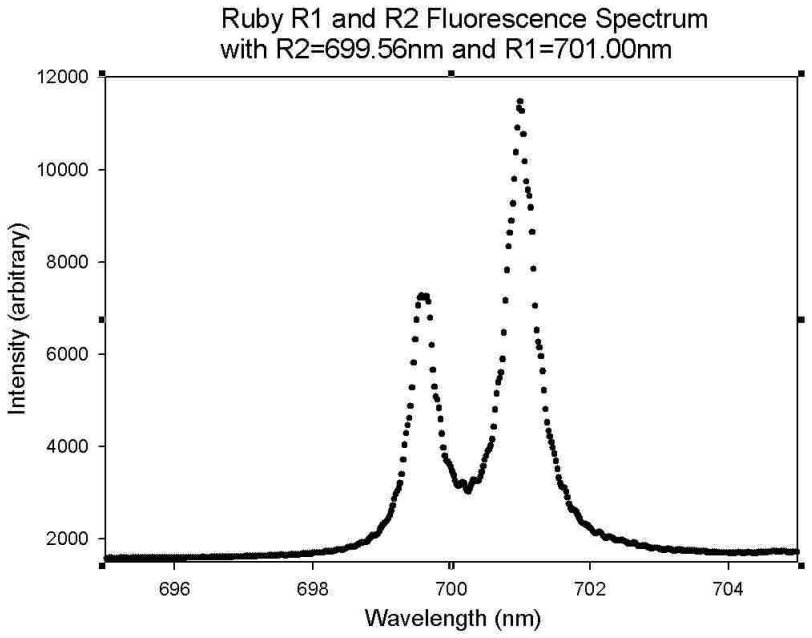

FIGURE 3.5: A measured ruby fluorescence spectrum of the $R1$ and $R2$ lines. For consistent calculation of the $R1$ line, one can fit a Voight function $V(\lambda)$ to the peak, taking λ_{R1} to be the value where $V_{max} = V(\lambda_{R1})$.

The ruby scale used for this experiment, proposed by [19], is given by

$$P_R = \frac{A}{B}\left[\left(\frac{\lambda}{\lambda_0}\right)^B - 1\right] \tag{3.1}$$

where $A = 1904$ and $B = 9.5$. A typical ruby fluorescence spectrum is shown in figure 3.2. The position (wavelength) of the $R1$ fluorescence line can be estimated by fitting a *Voigt* function (a superposition of Gaussian and Lorentzian profiles) to the measured fluorescence peak, the $R1$ position being the wavelength at the maximum value. This value for $R1$ may then be plugged into the above equation to calculate pressure in the sample chamber.

Takemura and Dewaele [20] determined an isothermal equation of state for gold using a helium pressure medium. As helium is the softest pressure medium over the largest pressure range, the results of this study are likely the most accurate for the gold $300K$ isotherm. A gold powder diffraction pattern may therefore be used to

calculate the pressure. Figure 4.1 shows a diffraction pattern of the sample Fe_3P with gold powder diffraction rings. The angular positions of the diffraction rings will change as pressure changes. Using the isothermal equation of state, we can predict the angular positions of the known reflections as a function of pressure; measuring the positions of these known reflections allows us to calculate the pressure. More on this will be discussed in the results and analysis chapter.

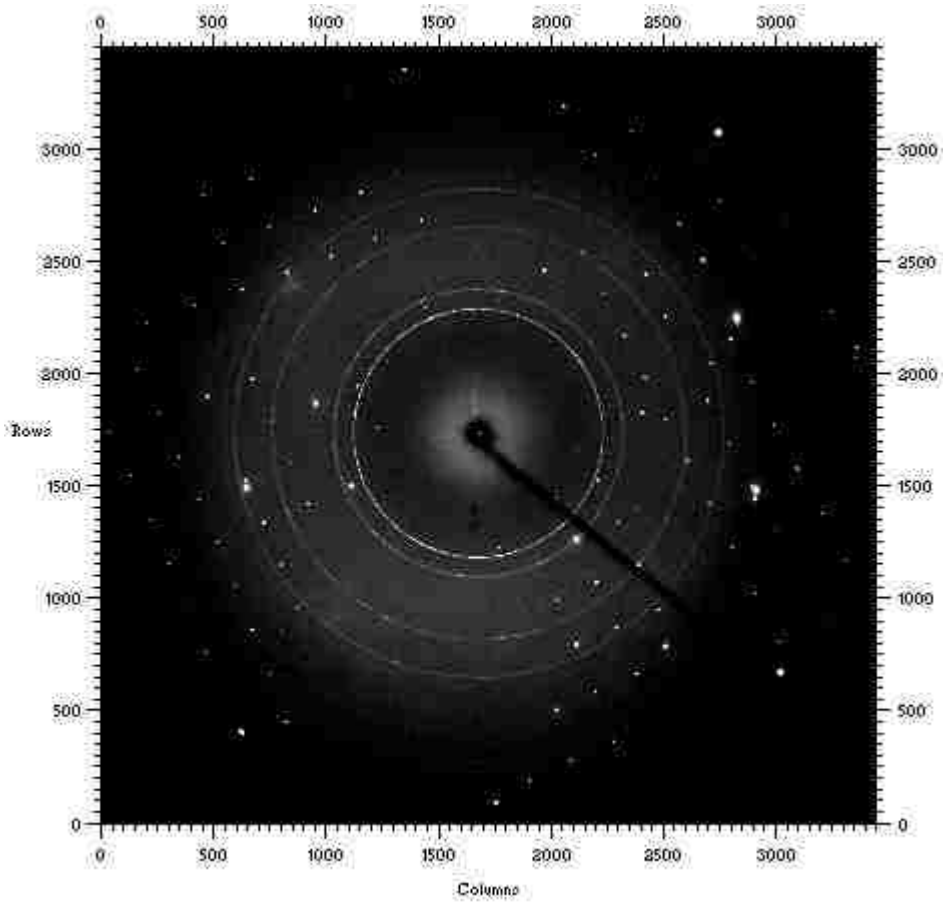

FIGURE 3.6: A diffraction pattern containing reflections from single crystal Fe_3P and gold powder. The positions of the gold powder rings will shift as pressure within the sample chamber changes.

3.3 High Pressure X-ray Diffraction

The source of x-rays and type of diffraction technique will determine the observed diffraction pattern. For continuous radiation and an area detector behind the sample perpendicular to the beam, many Laue equations will simultaneously be satisfied, resulting in a large number of reflections for an arbitrary orientation. The resulting pattern is known as a *Laue pattern*, and is useful for both structural and orientational determination.

For a monochromatic source, few (if any) reflections will be recorded for a given orientation. It is necessary to rotate the crystal with respect to the beam in order to satisfy more Bragg conditions, yielding more reflections (doing this with a continuous source would smear the reflections). The reflections yield pertinent information regarding the crystal's integrity; the more we have, the better our understanding of the crystal. In the case of this thesis a monochromatic source was used, and the sample was rotated during exposures.

Conventional x-ray diffraction has the advantage of using the full three-dimensional rotational freedom of the free crystal in order to record as many reflections as possible, while also investigating the crystal's long range uniformity. A *diffractometer* is an instrument used to orient the crystal and record its diffraction pattern at various positions and rotations. The rotating device is known as a *goniometer*, and the x-ray detection is an *area* or *CCD* detector (an area detector was used in the collection of data for this thesis).

For crystal samples under high pressure in a diamond anvil cell, we do not have the ability to position the crystal at an arbitrary angle. The sample is considerably small, and various components of the DAC obstruct the incident and diffracted beams. Even for specially designed DACs, the angular freedom one can rotate the sample is quite limited, thus the number of reflections one can record are limited as well. Figure 3.3 shows schematically a setup for high pressure diffraction experiments.

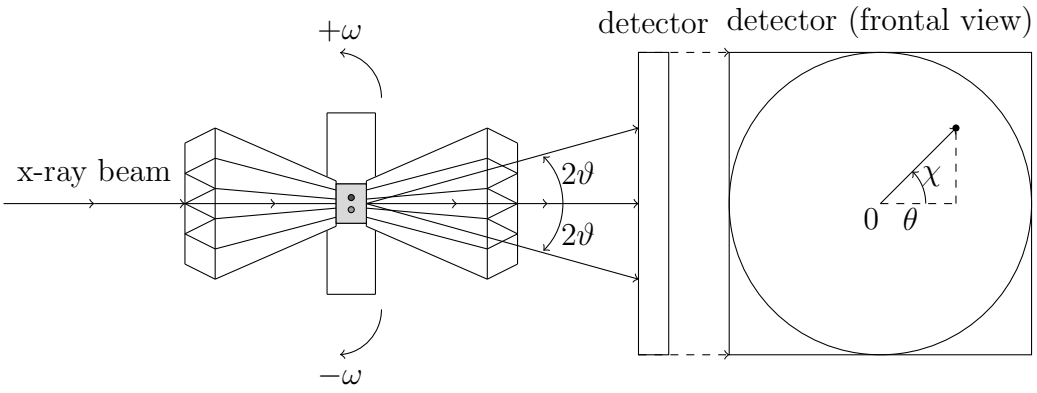

FIGURE 3.7: A simple schematic of a high pressure x-ray diffraction experiment. Incident x-rays bombard the sample within the sample chamber located a distance D from the area detector. The DAC can be translated and rotated within some angular range about the ω axis without obstruction by the diamond cell. Rotating the sample about an axis perpendicular to the beam axis allows for more reflections to be recorded on the area detector.

Instrumental calibration is necessary for accurate determination of the d-spacings corresponding to each reflection. This calibration includes the orientation of the detector with respect to the sample, the distance to the sample, and planar coordinates of the beam in the laboratory reference system. This calibration allows one to measure three angles (ω, θ and χ) of a reflection (with some Miller index hkl) and calculate its d-spacing ($d(hkl)$) using Bragg's law. For the calibration we use a sample with well known reflections and record its diffraction pattern; the wavelength is known. This allows us to make a correspondence between the pixels of the area detector and the scattering angle 2ϑ.

3.4 Experimental Specifics

This section will discuss the methods and procedures presented in the previous section in the context of this experiment. For the diamond cell this includes the size of the diamond culets, gasket thickness and hole diameter, spring (Belleville) washer arrangement, diamond seats, sample size, pressure markers and medium. The use of single crystals and acquisition of single crystal Fe_3P will be discussed. The

diffractometer specifics will be presented as well, including the calibration method.

The samples used were obtained from Alpha Aesar chemical supply company ; samples of single crystal Fe_3P were selected and examined prior to experimental runs to test for crystal integrity (see chapter 4). As opposed to powder diffraction, single crystal diffraction patterns reveal the long range nature of the crystal. Stress and strain, as well as observable phase transitions, are easily detected using single crystal methods. If large pressure gradients cause some crystallites to transition to another phase, and some to remain in the same phase, the resulting pattern will be a convoluted contribution of two species. Each reflection represents the spacing of a single atomic plane, whereas a powder diffraction ring yields the contributions from a large number of smaller single crystals, causing peak overlay; peak overlay represents an average of crystal plane spacing, not allowing for a complete structural analysis.

A symmetric diamond anvil cell [21] similar to that shown in figure 3.1 was used for this experiment. The diamond culets were $300\mu m$ in diameter, and the gasket thickness was $52\mu m$. The sample size was roughly $30\mu m$ in length, measured using microscope tick marks. The drill bit diameter (thus the gasket hole) was $120\mu m$. A 4:1 ratio of methanol:ethanol was used as the pressure medium, and gold powder was used as the pressure marker. Each screw used a Belleville washer arrangement of 36 washers, alternating directions for every 6 washers (figure 3.4 shows this schematically).

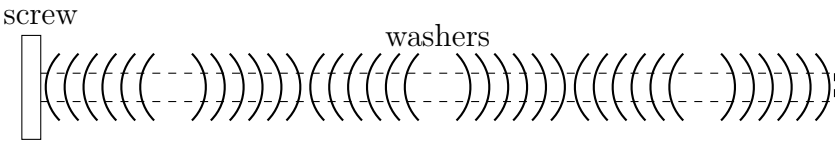

FIGURE 3.8: A schematic of the washer arrangement used in this experiment. Assuming a spring constant k for each washer, we have an effective spring of constant $\kappa = \frac{k}{\frac{1}{6}+\frac{1}{6}+\frac{1}{6}+\frac{1}{6}+\frac{1}{6}+\frac{1}{6}} = k$. By accounting for the contributions from each screw (essentially springs in parallel, $k_{total} = k_1 + k_2 + k_3 + k_4 = 4k$), one can estimate the force applied to the sample chamber.

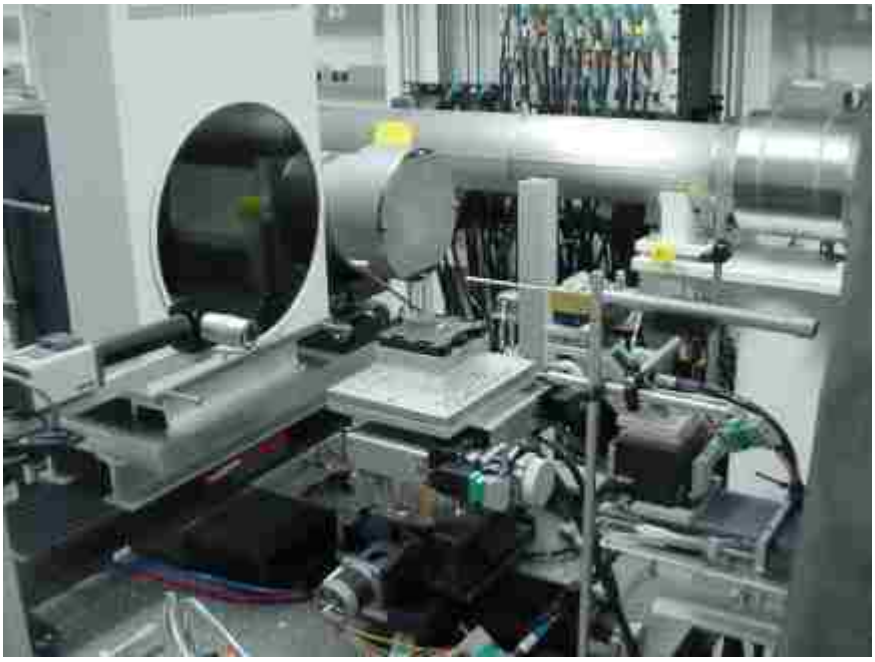

FIGURE 3.9: A picture of the ID-B experimental hutch of the APS at Argonne National Laboratory. The detector is seen on the left, the sample stage (no cell mount on stage) in the middle, and the pinhole (beam exit) just above the sample stage. During experimental runs, the sample stage contains a cell mount to properly position the loaded DAC. The stage can translate in the x, y and z directions, as well as rotate about an axis ω perpendicular to the beam axis

High pressure diffraction experiments were performed at sector 16 ID-B (insertion device) of the Advanced Photon Source at Argonne National Laboratory. Figure 3.4 shows a picture of the experimental hutch. At this station, electrons pass through an undulator causing high brilliance emission of x-rays and a narrow energy bandwidth of several harmonics. The x-rays are focused and the incident energy was $E = 33.69keV$ (resolution $\sim 10^{-3}$), corresponding to a wavelength of $\lambda = 0.368(\mathring{A})$. The area detector used in these experiments was a MAR 3450 image plate. The number 3450 signifies the number of pixels along each of two perpendicular axes (x and y Cartesian coordinate system); a total of 3450^2 pixels in all. Each pixel is $100\mu m$ in length (in both x and y). A cerium dioxide powder diffraction pattern was taken, and Fit2D powder diffraction software [22] was used to calibrate the detector. Figures 3.4 and

FIGURE 3.10: Fit2D interface at startup. 3450 is entered for the number of arrays corresponding to the number of pixels in the x and y directions (MAR 3450 image plate).

3.4 show the Fit2D interface. Figure 3.14 shows the diffraction pattern of CeO_2 powder used to calibrate the detector coordinates.

Calibration of the image plate requires one to use a known material and use its diffraction lines. Figure 3.4 shows the diffraction pattern of CeO_2 in the Fit2D interface. Clicking on the "calibrant" option allows one to enter known values and the software calculates and refines calibration parameters ([22] contains specific details of the Fit2D calibration process).

Next the calibration parameters are entered. One must open a file and click on the "integrate" option. This brings the screen on the left in figure 3.13. Once these parameters are entered, clicking "OK" will bring up another screen shown on the right in figure 3.13. These parameters likely do not need to be changed, and clicking "OK" once more performs the integration in 2ϑ space and makes a plot of intensity

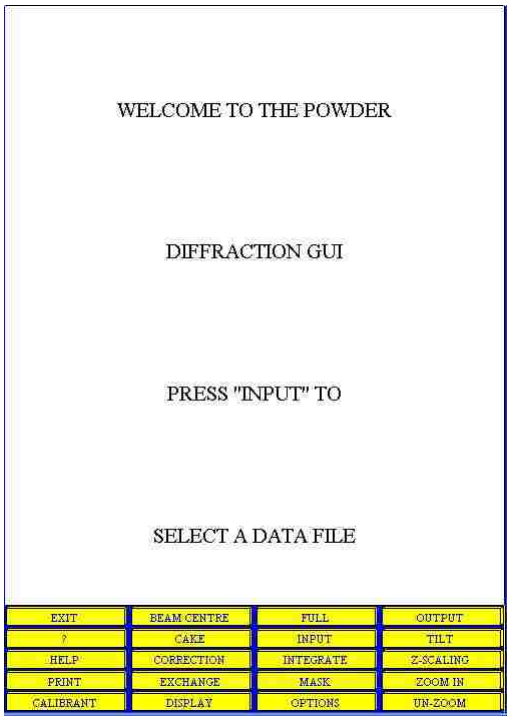

FIGURE 3.11: Fit2D interface showing the various options. Input allows one to select a file to open for viewing. Other options include calibration, changing the color, contrast, brightness, angular integration, etc.

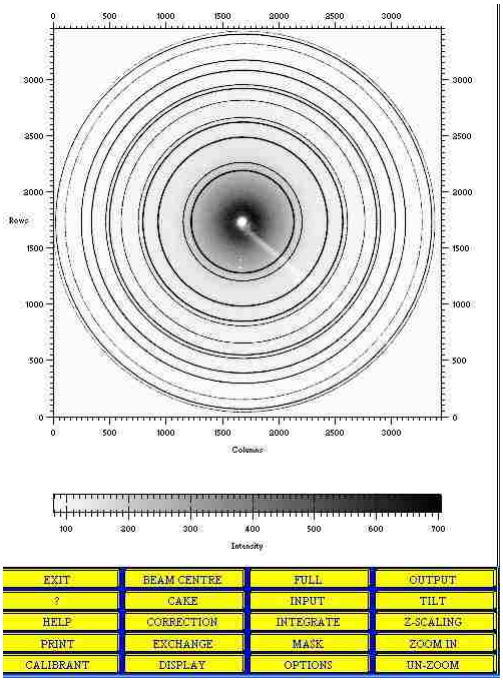

FIGURE 3.12: Fit2D interface showing the diffraction pattern of the CeO_2 calibrant used in this experiment various options. This file is viewed by clicking the "input" option and selecting the file from a list.

versus 2ϑ. Clicking the "exchange" option allows one to toggle between the diffraction pattern and the two-dimensional intensity versus 2ϑ plot. Figure 3.14 shows the diffraction pattern for CeO_2 and its angular integration plot for this experiment. A good calibration is established by using the "cake" option in Fit2D; the details of this procedure can be found in [22]. The calculated calibration function should agree well with each of the known values of the measured CeO_2 peaks. If not, the calibration procedure must be repeated. Data collection and analysis was performed after adequate detector calibration.

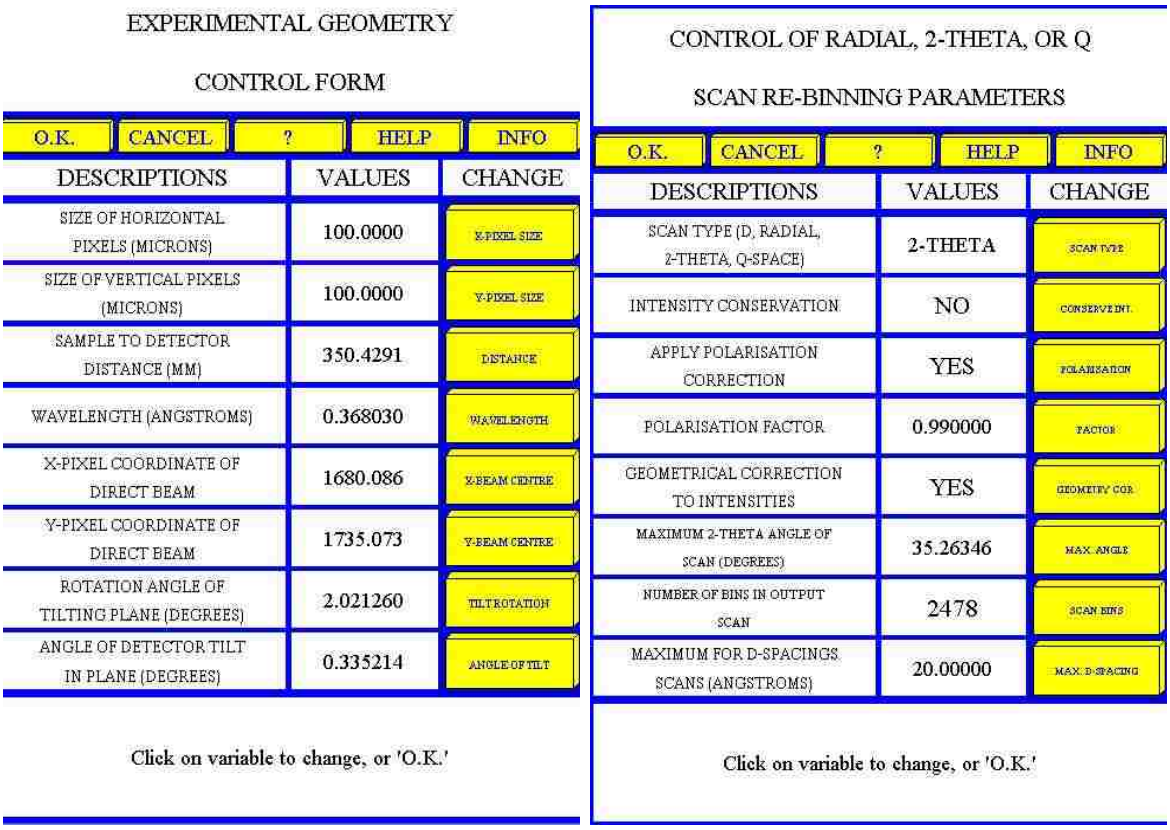

FIGURE 3.13: Fit2D integration interface. Calibration parameters are entered on the left. Clicking "OK" brings up the screen on the right, which are settings for the transform calculation. Clicking "OK" once more performs the calculation and plots the intensity versus 2ϑ. These are the values used for experimental analysis.

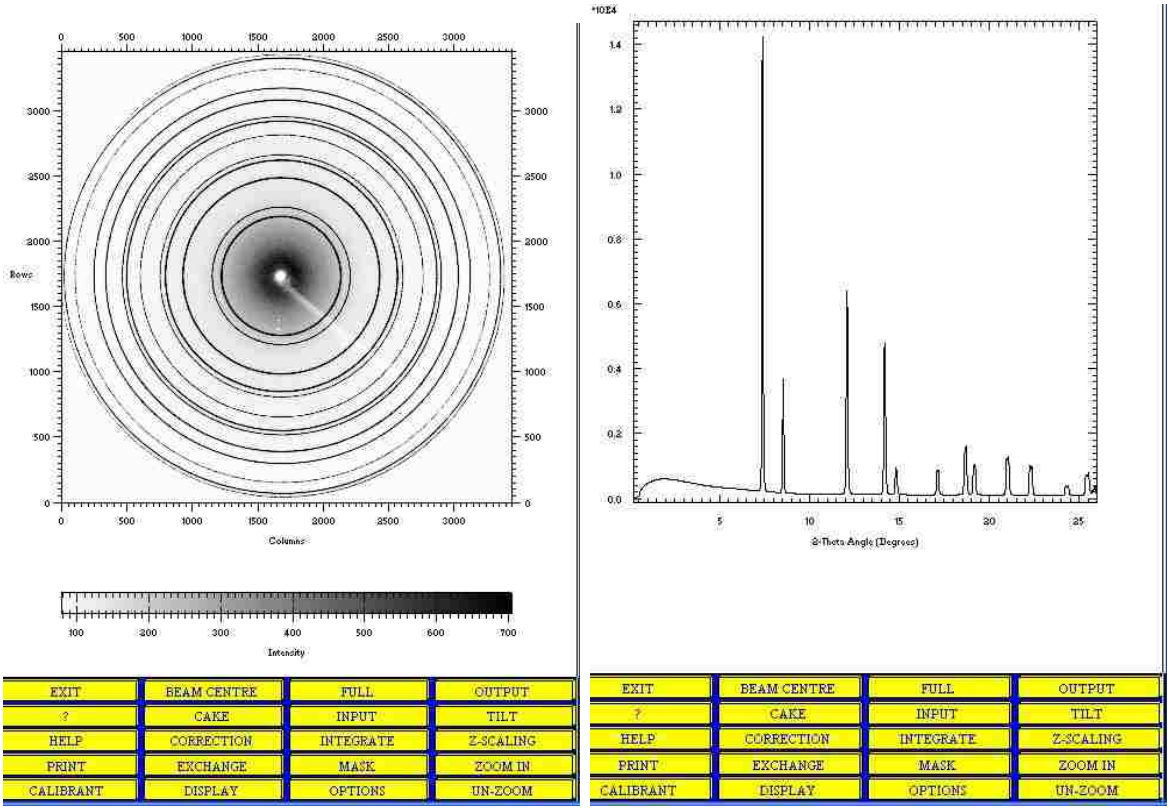

FIGURE 3.14: The diffraction pattern and angular integration of CeO_2 calibrant as viewed in the Fit2D interface. Positions of known reflections allow us to calibrate the sample to detector distance, detector orientation, and $x - y$ coordinates of the pixels. The (x, y) position x-ray beam is designated as the origin.

CHAPTER 4

RESULTS AND ANALYSIS

This chapter serves to present an analysis of the raw data collected in this experiment. The raw data are 20 second exposure MAR 3450 image plate files. Fit2D [22] software was used to analyze and export data to other programs such as Sigmaplot [23] and X-ray Helper [24] for peak location and pressure calculations. Sigmaplot and Unit-cell [25] were used for plotting and regression analysis. Error analysis is discussed at the end of this chapter.

4.1 Sample Identification and Specification

Before loading a sample with pressure medium in the DAC, it is important to ensure that a good crystal is chosen. We place a tentative sample and pressure standard in the sample chamber without pressure medium and take a diffraction pattern. This allows us to identify the sample as Fe_3P while also checking that our pressure standard gives the correct reading at atmospheric pressure. Exposures of two different crystals at atmospheric pressure and $300K$ (within the sample chamber) are shown below in figure 4.2. We can see some regularity of reflections in several regions in the diffraction pattern, as well as Debye-Scherrer rings from gold pressure standard and several intense reflections from the diamonds. Figure **??** shows magnified portions of the image plate to show the spatial periodicity of reflections.

After taking the initial exposure, we wanted to verify that Fe_3P is the sample in the DAC. This was done by calculating the predicted d-spacings based on known unit cell parameters of Fe_3P. Table 4.1 shows the unit cell parameters of Fe_3P under ambient conditions for two independent data sets.

X-ray Helper software designed by [24] allows one to simultaneously open chi files (ascii format) of measured diffraction data (using a monochromatic source) and peak position files of known materials. A quick comparison of these two spectra

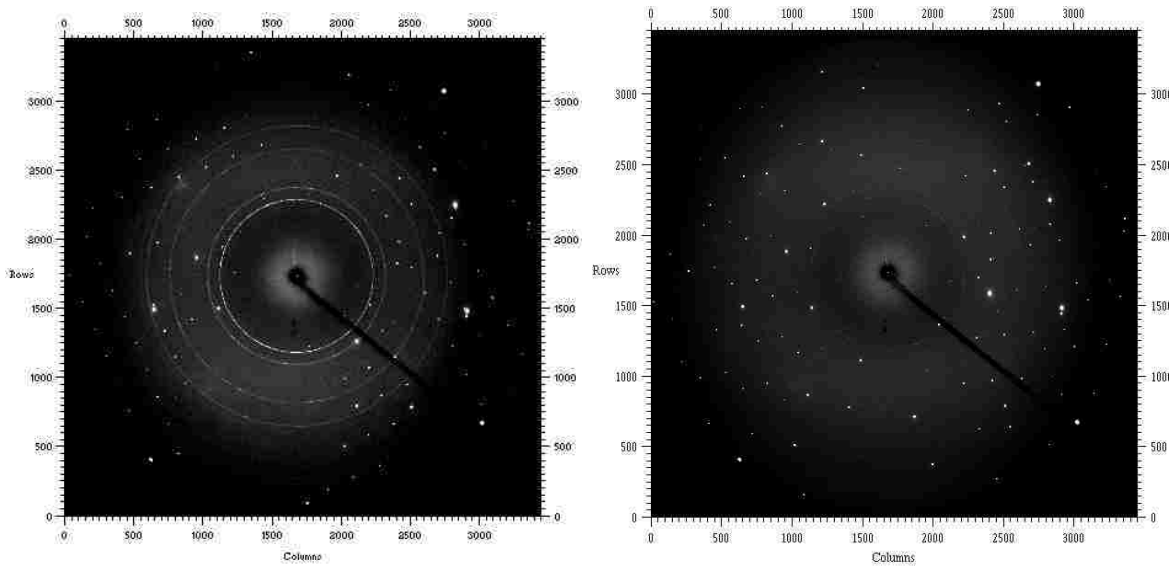

FIGURE 4.1: Diffraction patterns of single crystal Fe_3P and gold powder at $300K$ and atmospheric pressure. The four intense peaks on the right side of each image are diamond reflections.

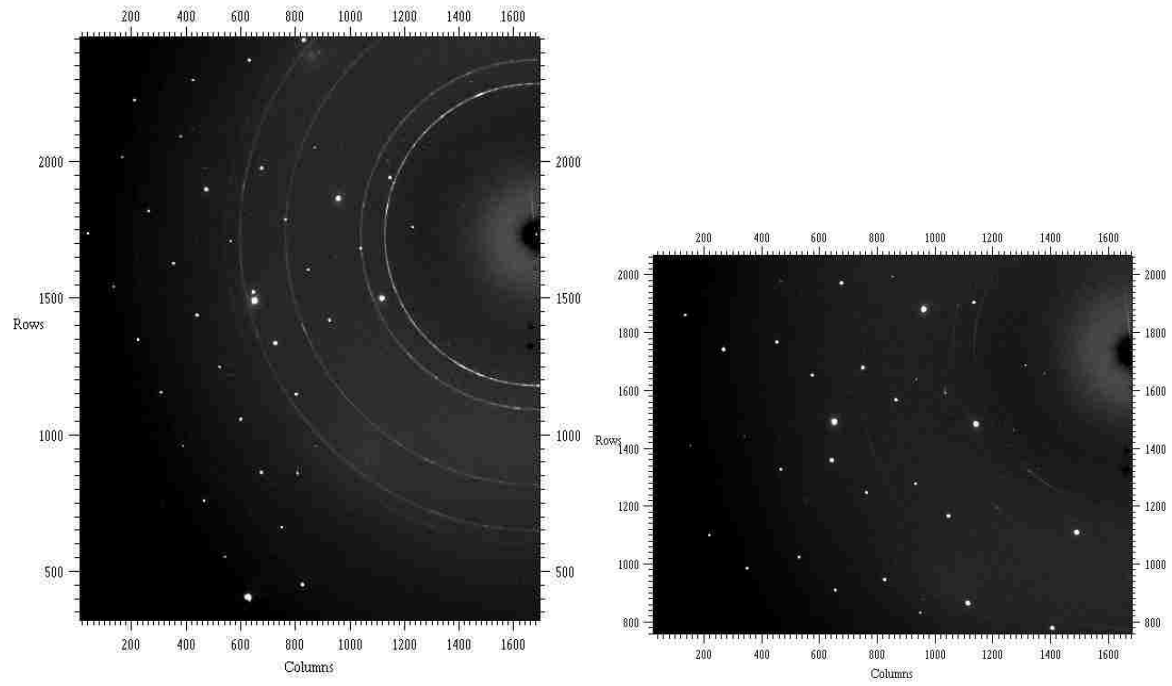

FIGURE 4.2: Zoomed in regions of diffraction patterns of single crystal Fe_3P and gold powder at $300K$ and atmospheric pressure. The different orientations of the crystals may be seen by the periodicity of reflections.

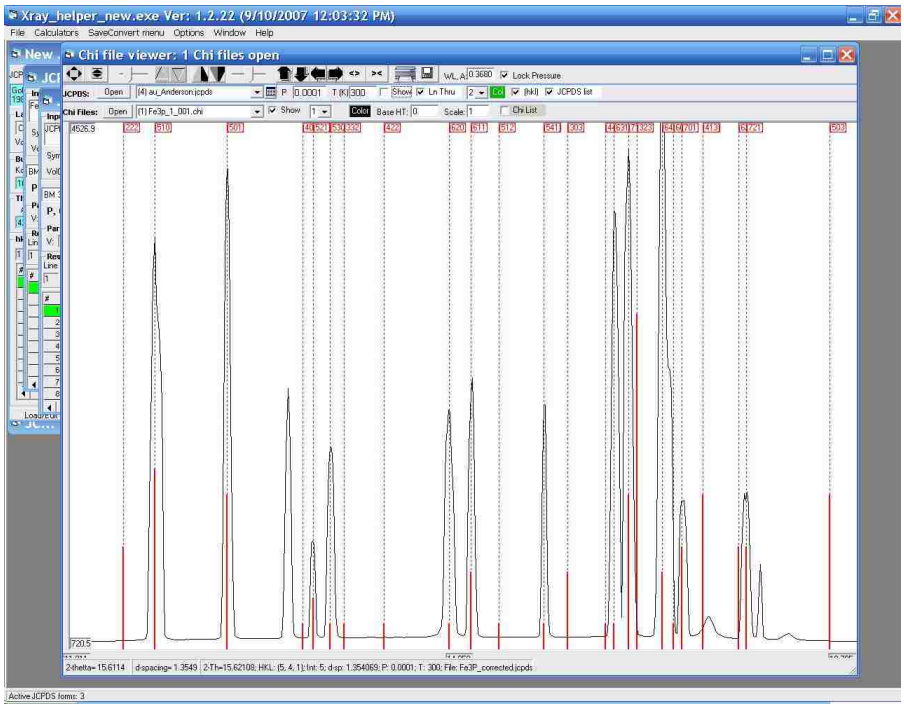

FIGURE 4.3: The measured pattern (continuous spectrum) and predicted positions (discrete spectrum) in 2θ space in X-ray Helper interface (zoomed in for clarity). The wavelength is set to $\lambda = 0.3680$Å and the pressure $P = 0.0001GPa$. One cannot fully distinguish contributions of Fe_3P from gold and diamond, as this integration is over the entire detector with no masks. This comparison is not intended for rigorous analysis, but for quick assurance that Fe_3P is indeed present.

allowed us to determine that the pattern belongs to Fe_3P. Figure 4.1 shows the X-ray Helper interface with a portion of the measured and predicted patterns under ambient conditions.

Figure 4.4 shows a diffraction peak as seen on the image file and its location in 2θ space. Using [23] we fitted a 5-parameter Voigt function

$$V = y_0 + a\left(c\left(\frac{1}{1+((x-x_0)/b)^2}\right)\right) + (1-c)\exp\left[-0.5((x-x_0)/b)^2\right] \qquad (4.1)$$

(where $x = 2\theta$) to each peak and took the 2θ that gives $V(2\theta) = V_{max}$ as the angular position of each reflection. This equation allows us to account for Lorentzian and Gaussian peak broadening, as well as the background (y_0 offset). Using the Bragg

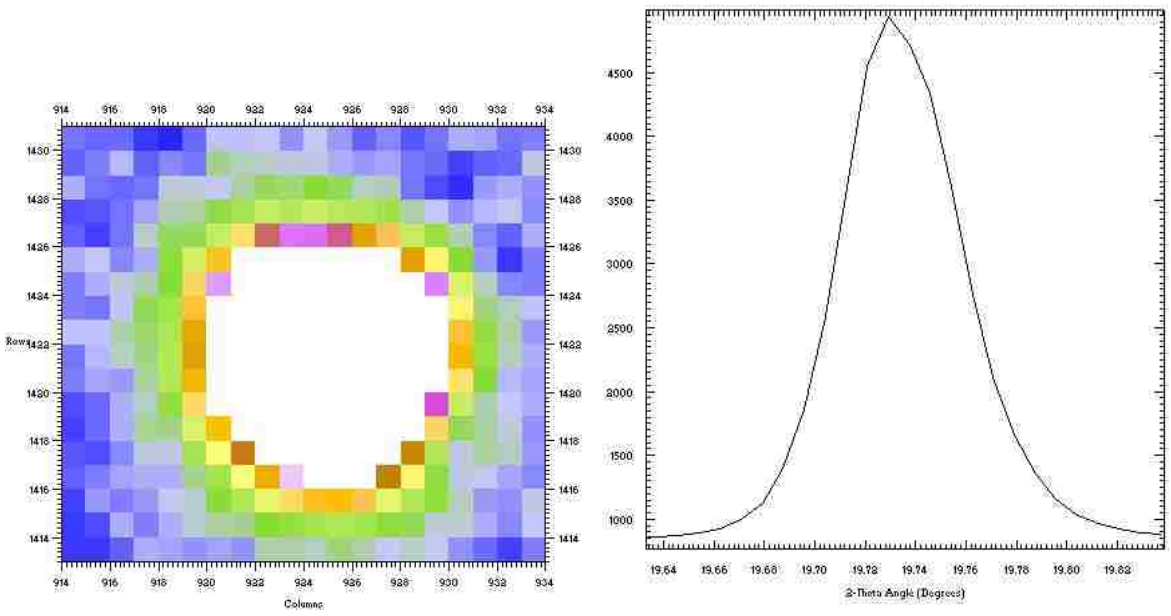

FIGURE 4.4: A zoomed in picture of a reflection and its integrated spectrum. The center of the peak is calculated by fitting a 5-parameter Voigt function of the form given in equation 4.1

equation we calculated d from $\lambda = 2d\sin\theta$. Next, we indexed (assigned a Miller index, hkl) each reflection belonging to the sample. It is important to note that for a tetragonal crystal, many reflections will occur at the same scattering angle θ (e.g. 220 and $\bar{2}20$), but at different (x, y) coordinates on the detector due to crystal symmetry. We treated each reflection separately, and compared its d-spacing with some possible predicted values. Knowing the unit cell parameters and lattice symmetry under ambient conditions [26], we calculated the expected d-spacings of possible reflections using $\frac{1}{d^2} = \frac{h^2+k^2}{a^2} + \frac{l^2}{c^2}$, allowing the various hkl to range from 0 to ± 10. We compared this list to the measured values of each reflection and looked for possible matches (In a powder diffraction pattern, individual reflections can not be resolved as the ring represents the overlap of contributions from all reflections occurring at that angle).

We listed the possibilities for each the Miller indices for neighboring reflections and deduced an adequate scheme in agreement with data observation. Figure 4.1 shows the diffraction pattern with corresponding Miller indices to the right. The

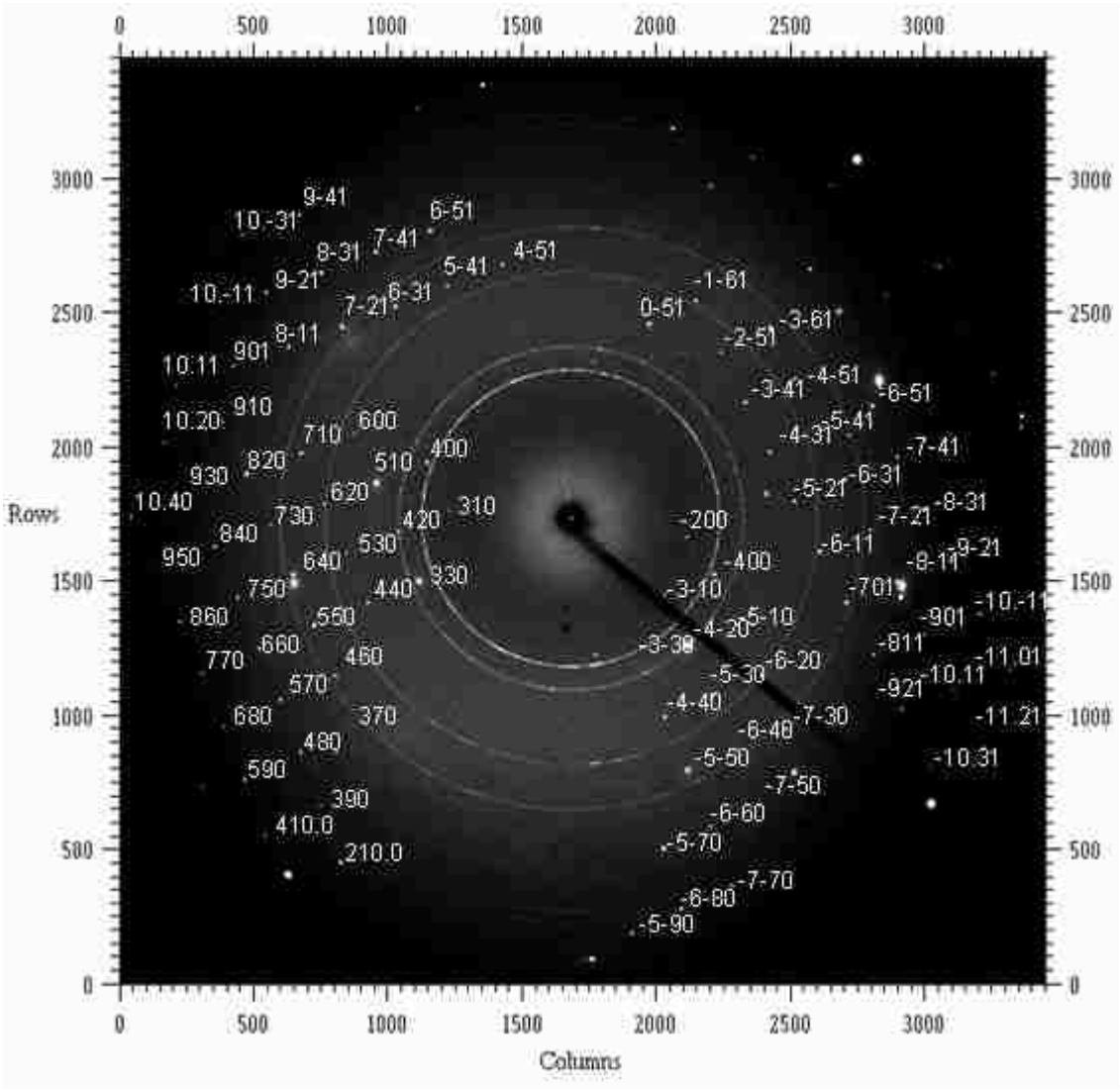

FIGURE 4.5: The indexed diffraction pattern of the sample under ambient conditions. Indices are assigned based on the comparison of possible Miller indices of adjacent reflections. Using the condition $h + k + l = 2n$ and the fact that d decreases with increasing θ, a scheme for the pattern is found by trial and error.

measured values of each reflection were in good agreement with predicted values, and a least squares refinement of the unit cell parameters gave good agreement with [27, 26] under ambient conditions; cell parameter determination will be discussed in detail in section 4.3.

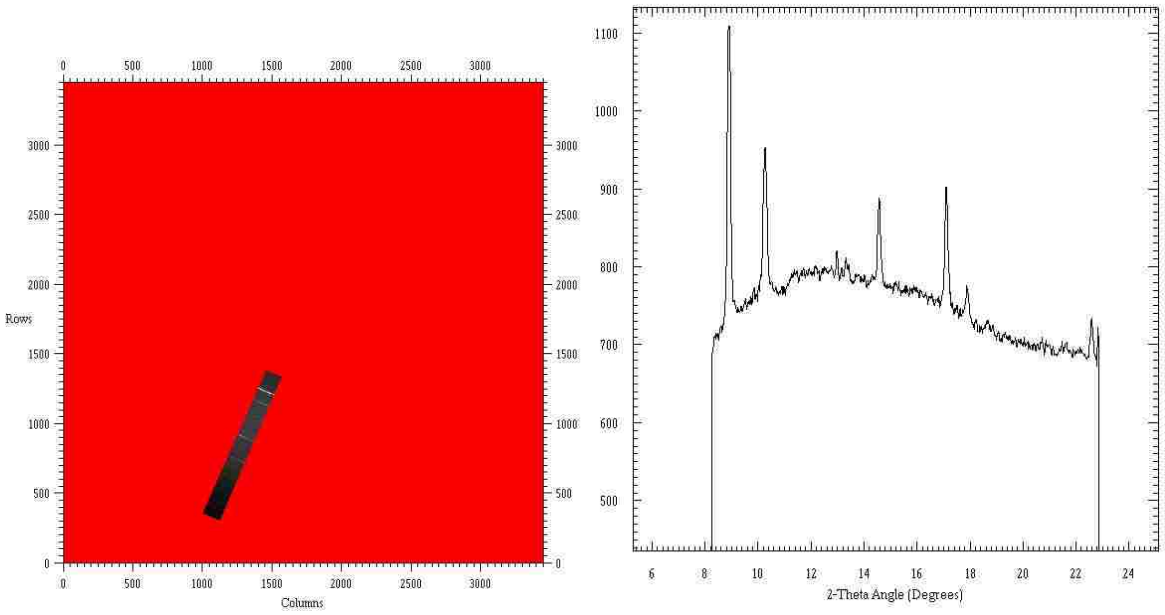

FIGURE 4.6: A slice of the diffraction pattern is selected and integrated; this is done using the "mask" option. The masked (red) portion contributes zero to the angular integration. This allows one to easily analyze the positions of the gold powder diffraction rings, without contributions from the sample or diamond that lie at the same angle.

4.2 Pressure Determination

A ruby was used to ensure the sample chamber was under pressure after initial load, and a gold powder standard was used for the duration of the experiment. Using characteristic diffraction lines of gold, and the P-V isotherm proposed by [20], the pressure in the sample chamber was calculated. Figure 4.6 shows the image file with the user defined masked next to its angular integration pattern. This allows us to analyze contributions from gold powder alone.

We can export the integrated file as a chi plot which is compatible with other data analysis software. This allows us to closely examine the angular positions in 2θ space. Figure 4.2 shows the above fit2D integrated pattern in the X-ray Helper interface. One can upload predicted peak positions files (e.g. JCPDS files) and chi plots (intensity vs. 2θ histograms) simultaneously for straightforward comparison. Equations of state may also be programmed so that the predicted peak positions

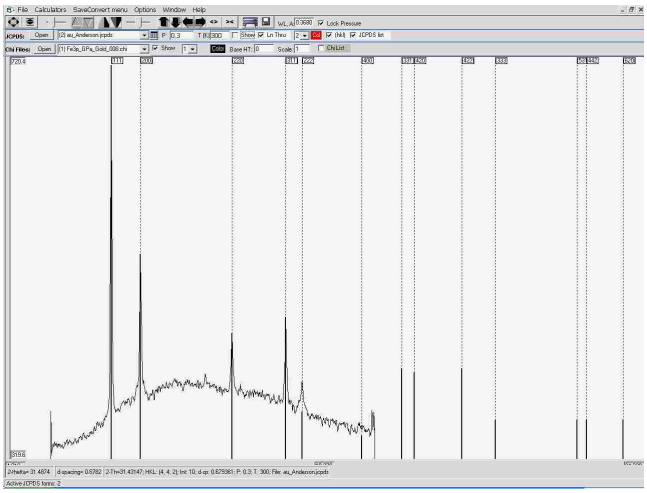

FIGURE 4.7: This graph shows the integrated pattern of the masked portion with known peak positions in the x-ray helper interface. One can implement an isotherm for a known material to calculate known reflection positions. In this case we use the isotherm proposed by [20] to calculate the positions of known reflections for a given pressure.

adjust as the appropriate pressure, temperature, and wavelength are entered.

Pressure (GPa)	Tetragonal			Triclinic						
	a(Å)	c(Å)	V(Å)^3	a(Å)	b(Å)	c(Å)	α (deg)	β(deg)	γ(deg)	V(Å)^3
0.0	9.116	4.43	368	9.103	9.102	4.43	90.1	89.60	89.90	367
0.2	9.106	4.41	366	9.095	9.092	4.42	90.2	89.60	89.90	367
1.5	9.081	4.38	361	9.070	9.079	4.40	89.7	89.72	90.07	364
3.2	9.050	4.35	356	9.058	9.055	4.38	89.8	89.79	89.88	367
4.5	9.030	4.33	353	9.034	9.028	4.34	89.8	89.60	89.91	367
6.1	9.011	4.54	369	9.001	9.003	4.51	90.1	89.77	89.90	369
7.8	8.971	4.32	348	8.966	8.958	4.31	90.0	89.75	89.86	349
8.7	8.964	4.30	345	8.955	8.961	4.32	90.1	89.60	89.90	347
10.5	8.93	4.30	343	8.91	8.90	4.33	90.0	89.66	89.87	344
12.5	8.93	4.31	344	8.92	8.90	4.34	90.1	89.59	89.95	345
14.4	8.91	4.29	341	8.88	8.90	4.33	89.6	89.70	89.92	343
16.0	8.90	4.28	339	8.87	8.85	4.30	89.7	89.58	89.90	341
17.6	8.89	4.27	337	8.85	8.83	4.31	90.1	89.60	89.84	339
18.3	8.88	4.26	336	8.84	8.85	4.31	89.3	89.77	89.81	337
19.6	8.87	4.24	334	8.85	8.86	4.28	89.4	89.66	89.89	337

Data Set (ambient conditions)	a(Å)	c(Å)
[3]	9.107	4.460
[26]	9.1	4.459

TABLE 4.1: A table showing the results from fitting the data to both a tetragonal and triclinic lattice. Below are the results of unit cell parameters (tetragonal refinement) determined from independent experiments. Values are reported to the appropriate number of significant digits.

4.3 Cell Parameter and Compressibility Calculation

By performing a nonlinear least squares fit of $\frac{1}{d^2}$ versus $\frac{h^2+k^2}{a^2} + \frac{l^2}{c^2}$, we determined the unit cell parameters a and c and there respective uncertainties at each pressure point, assuming the symmetry is tetragonal. If the symmetry remains tetragonal over a measured pressure range, we expect a P-V relationship of the form given by [11] over this range. We also relieved symmetry constraints by fitting the data to a triclinic lattice for comparison.

Table 4.1 lists the various cell parameters for both tetragonal and triclinic refinements of the experimental data. Disagreement between cell parameters a and c between fits give a measure of how the sample was strained. Angles α, β and γ should be 90° within uncertainties if sample is truly of tetragonal symmetry.

Above 10 GPa, the methanol/ethanol pressure medium becomes very stiff, and large pressure gradients within the sample chamber are sustained. Figure 4.19 shows

Data Set	Pressure (GPa)	$a(\mathring{A})$	$c(\mathring{A})$
Scott et al	0.0000	9.0990	4.4630
	0.2	9.098	4.460
	0.5	9.092	4.454
	0.7	9.094	4.454
	1.2	9.080	4.448
	2.4	9.063	4.436
	2.7	9.056	4.434
	3.5	9.037	4.427
	3.7	9.032	4.429
	4.4	9.023	4.419
	5.2	9.013	4.412
	5.6	9.004	4.410
	6.2	8.994	4.408
	6.5	8.986	4.402
	6.8	8.988	4.402
	7.4	8.976	4.394
	9.1	8.959	4.385
	9.5	8.943	4.389
	9.9	8.937	4.395
	10.0	8.952	4.378
	11.0	8.943	4.374
	12.3	8.92	4.38
	12.4	8.914	4.371
	12.8	8.91	4.36
	13.6	8.89	4.37
	14.5	8.92	4.33
	15.5	8.87	4.373
	16.7	8.84	4.350
Dera and Lavina	19.1	8.8155	4.3132
	21.8	8.7711	4.3077
	23.0	8.7563	4.3109
	27.0	8.7047	4.2832
	31.0	8.6534	4.2774
	34.1	8.6087	4.2604
	37.2	8.5684	4.2378
	41.0	8.5423	4.2357
	52.2	8.4460	4.1982
	62.0	8.3764	4.1652

TABLE 4.2: A table of unit cell parameters a and c reported by independent experiments. The data collected by Scott et al used a powdered sample, and the experiment of [28] used single crystals grown from an independent researcher. Values are reported to the number of significant digits reported from each data set.

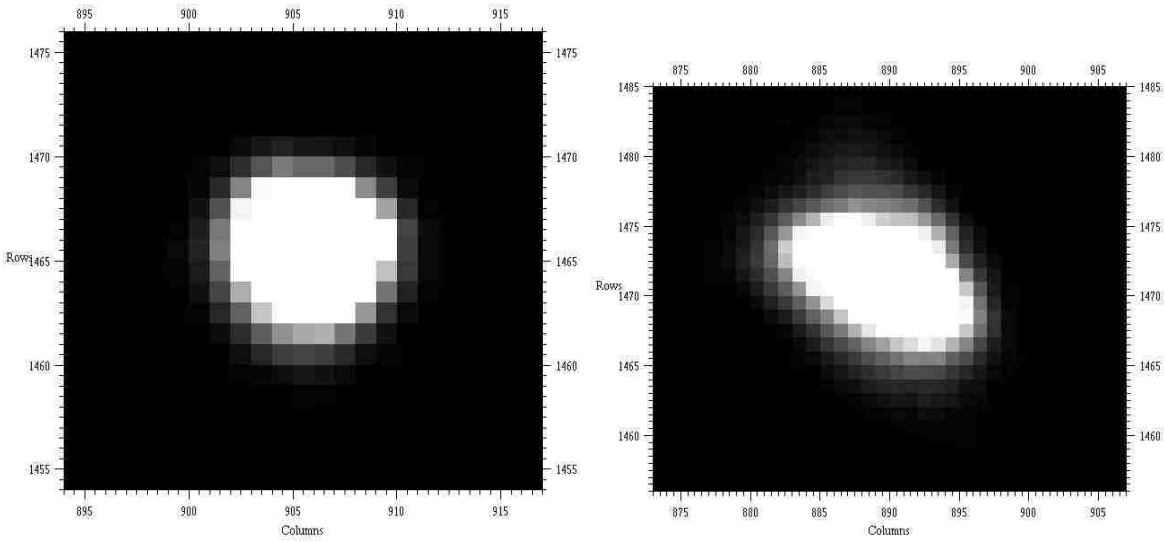

FIGURE 4.8: Peak profiles of the 440 reflection Fe_3P at 8.7 GPa (left) and 10.5 GPa (right). Distortion in diffraction peak due to hardening of methanol ethanol pressure medium above 10 GPa is apparent in most reflections.

the profile of diffraction peaks below and above this pressure. The conditions are no longer hydrostatic, as this is evidenced by distortion in peak profile and large disagreement between d-spacings of like reflections. Increasing pressure beyond this point further distorts the crystal, the peaks eventually spreading out over 10's of pixels in the x and y directions at the highest pressure. Table 4.3 shows the parameters determined from fitting equations 1.4 and 1.13 to each data set separately. Ideally, these parameters should agree within experimental uncertainty. Good agreement is found between fit parameters of the same data set, but there is a large discrepancy between the results of this study and those of [27] and [28], aside from V_0. Aside from V_0, K_0 and K_0' have relatively large uncertainties.

In an attempt to better constrain K_0 and K_0', we used two alternate approaches. Using the high pressure data collected by [28], and values of the cell parameters a and c under ambient conditions (from this study and [3]), we fit both 2 and 3 parameter isotherms using the Vinet and Birch-Murnaghan formulations. Also, we calculated the axial compressibilities at zero pressure by performing a linear fit to each data set

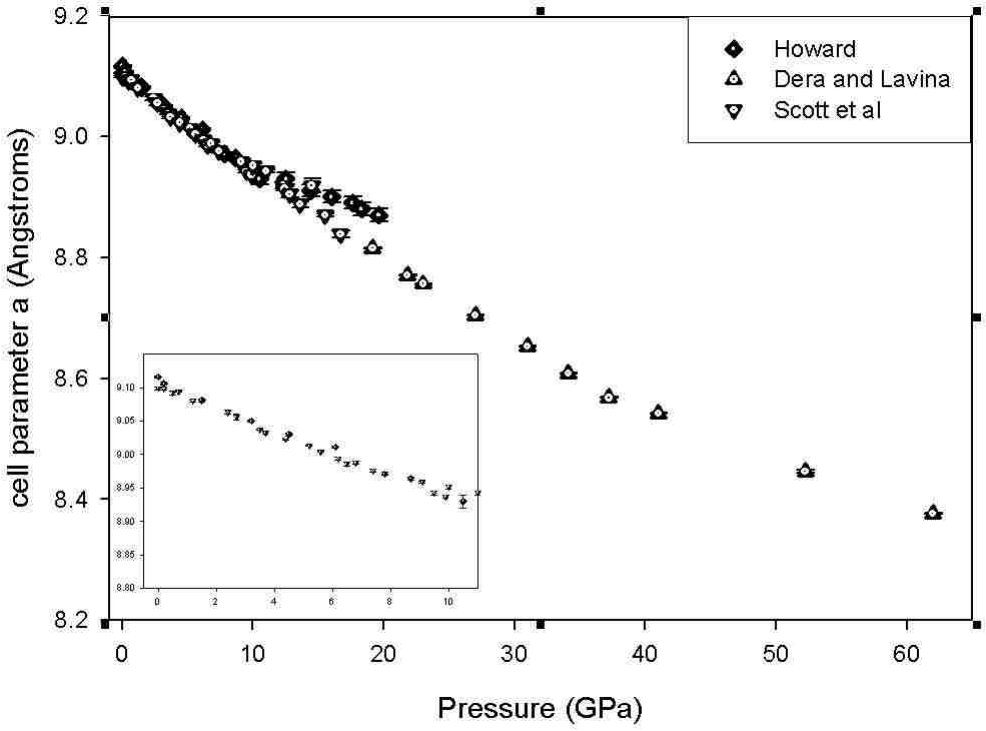

FIGURE 4.9: Plot of cell parameter a versus pressure. Inset shows hydrostatic data from $0 - 10GPa$. We observe that a decreases linearly with increasing pressure up to about 10 GPa, jumps horizontally, then follows a different linear trend up to 20 GPa. This jump is likely due to the hardening of the methanol/ethanol pressure medium near this pressure [17], which causes large pressure gradients within the sample chamber. Reflections in the diffraction patterns become broader above this pressure, thus the uncertainty in a becomes significantly larger.

Data Set	$P_{ave}(GPa)$	$\frac{\Delta c}{\Delta P}\frac{1}{c_{ave}}$ (1/GPa)	$\frac{\Delta a}{\Delta P}\frac{1}{a_{ave}}$ (1/GPa)
	0.10	5.5e-3	0.015
Howard	0.85	2.1e-3	5.3e-3
	2.35	2.0e-3	4.0e-3
	3.85	3.2e-3	6.6e-3
	5.30	1.3e-3	-3.0e-4
	6.95	2.6e-3	3.2e-4
	8.25	8.7e-4	5.2e-3
	9.60	2.1e-3	0.0
	11.50	0.0	-1.2e-3
	13.45	1.1e-3	2.3e-3
	15.20	7.5e-4	1.6e-3
	16.80	7.0-4	1.5e-3
	17.95	1.6e-3	3.3e-3
	18.95	8.7e-4	3.6e-3

TABLE 4.3: A table of the compressibilities of a and c calculated from the unit cell parameters determined from data collected in this study. The *ave* subscript denotes the average between two adjacent data points, and Δ denotes their difference.

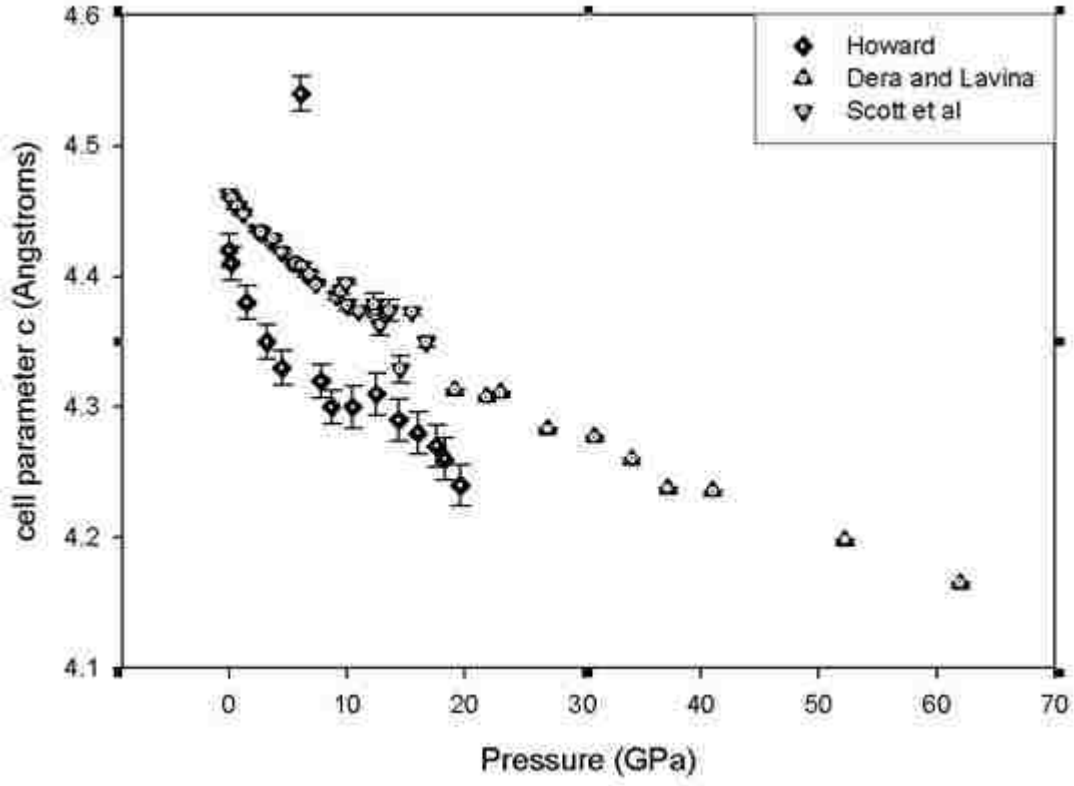

FIGURE 4.10: Plot of cell parameter c versus pressure. We observe that c decreases linearly with increasing pressure up to about 5 GPa, increases around 6 GPa, then decreases. The increase of c at 6 GPa is unexpected, and is likely due to an unacknowledged source of uncertainty. It is not physical for the unit cell parameters (thus the volume) to increase with increasing pressure. The characteristic stiffening (of the methanol/ethanol pressure medium) near 10 GPa is expected and observed.

Data Set	P_{ave} (GPa)	$\frac{\Delta c}{\Delta P}\frac{1}{c_{ave}}$ (1/GPa)	$\frac{\Delta a}{\Delta P}\frac{1}{a_{ave}}$ (1/GPa)
Dera and Lavina	20.48	1.9e-3	4.8e-4
	22.41	1.4e-3	-6.3e-4
	25.00	1.5e-3	1.6e-3
	29.00	1.5e-3	3.4e-4
	32.57	1.7e-3	1.3e-3
	35.67	1.5e-3	1.7e-3
	39.11	8.0e-4	1.3e-4
	46.61	1.0e-3	7.9e-4
	57.11	8.5e-4	8.1e-4

TABLE 4.4: A table of the compressibilities of a and c calculated from the unit cell parameters determined from data collected by [28]. The *ave* subscript denotes the average between two adjacent data points, and Δ denotes their difference.

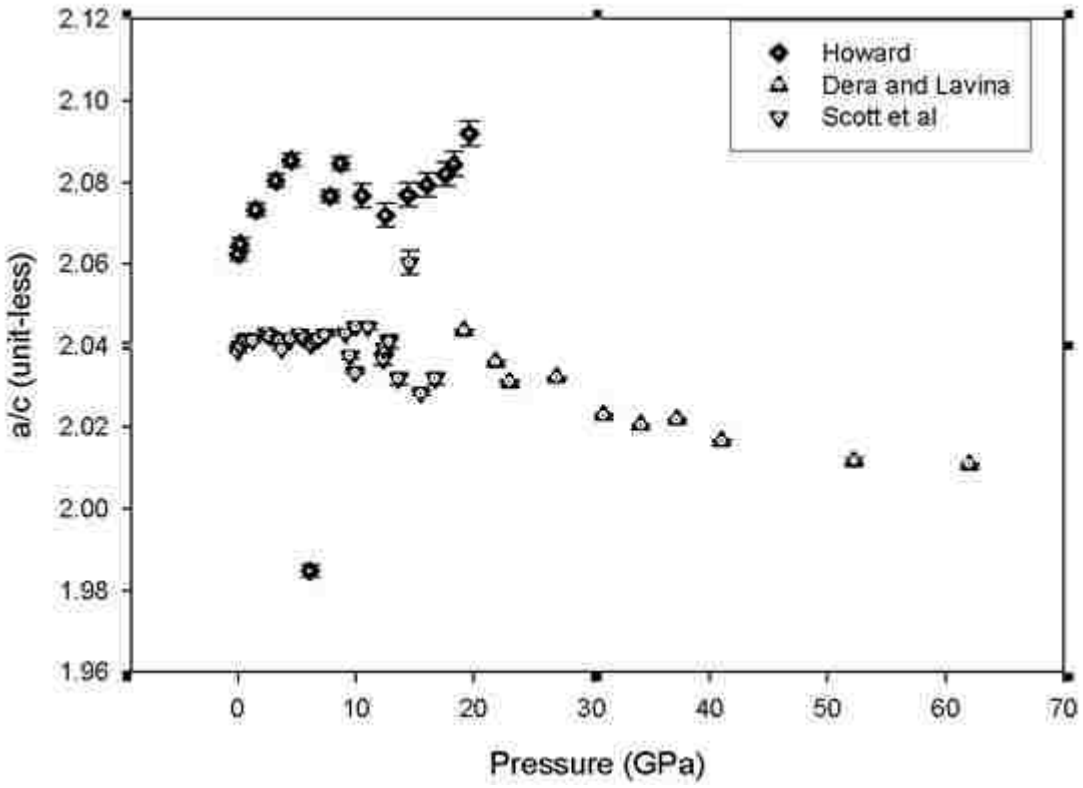

FIGURE 4.11: A Plot of the ratio $\frac{a}{c}$ versus pressure. Near 6 Gpa we observe a sharp change in this ratio, but this is due to the anomaly in c at this pressure.

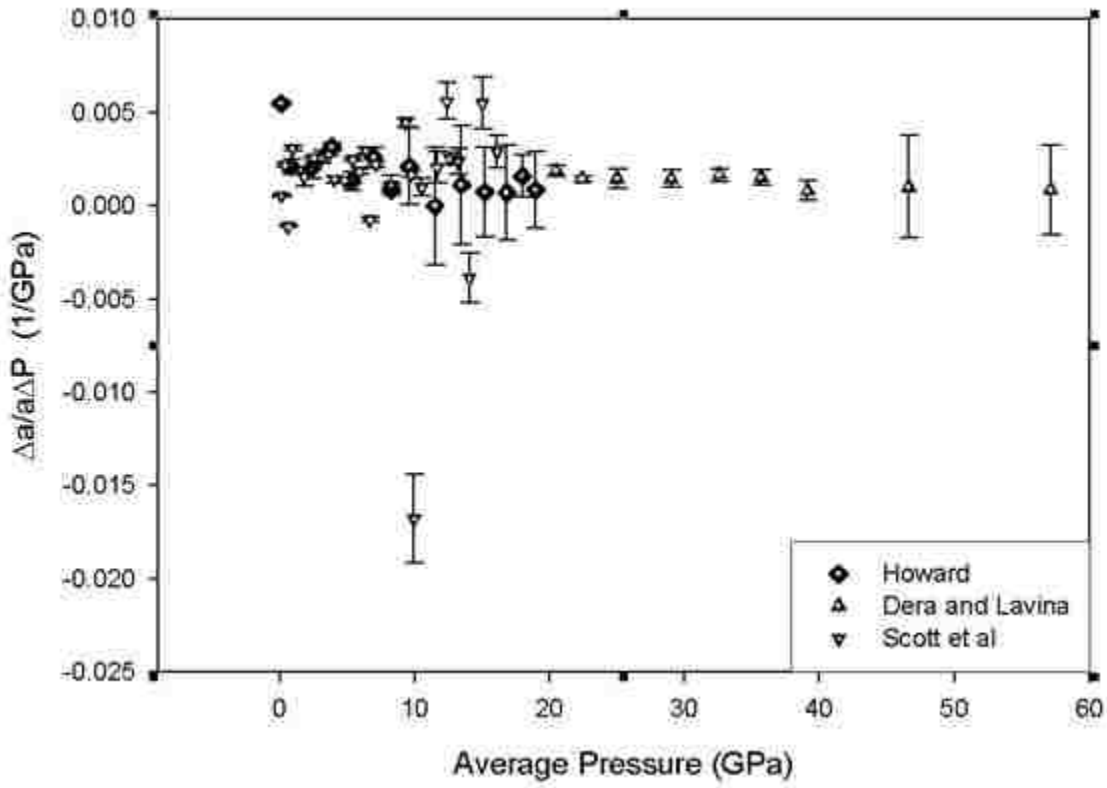

FIGURE 4.12: A Plot of the axial compression of cell parameter a versus average pressure.

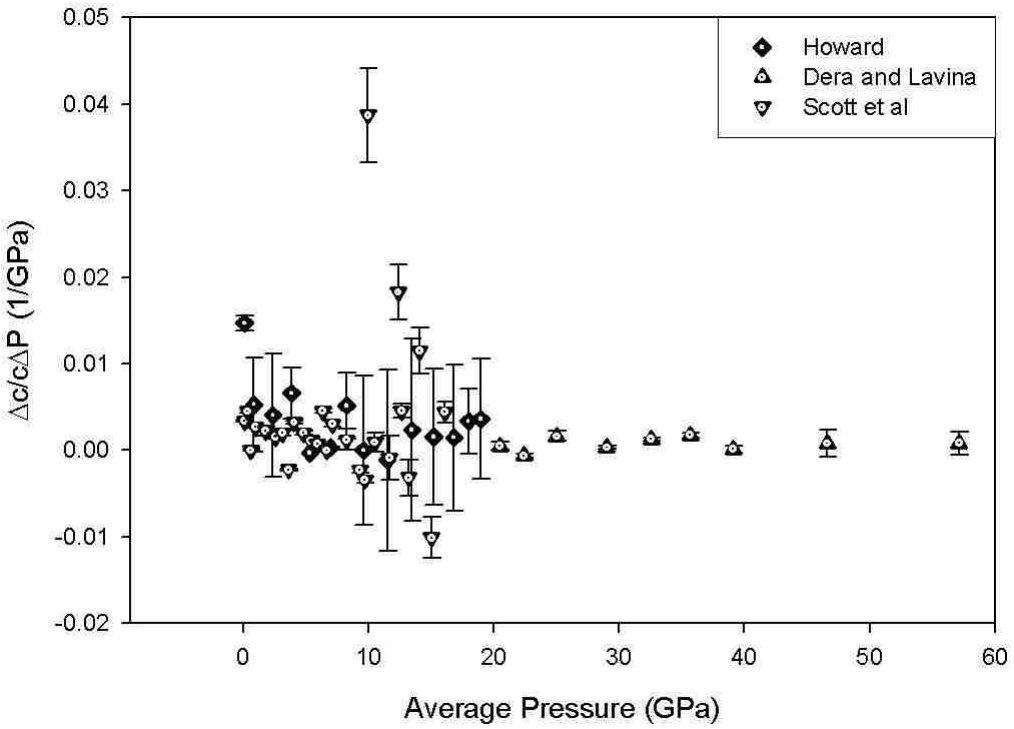

FIGURE 4.13: A Plot of the axial compression of cell parameter c versus average pressure.

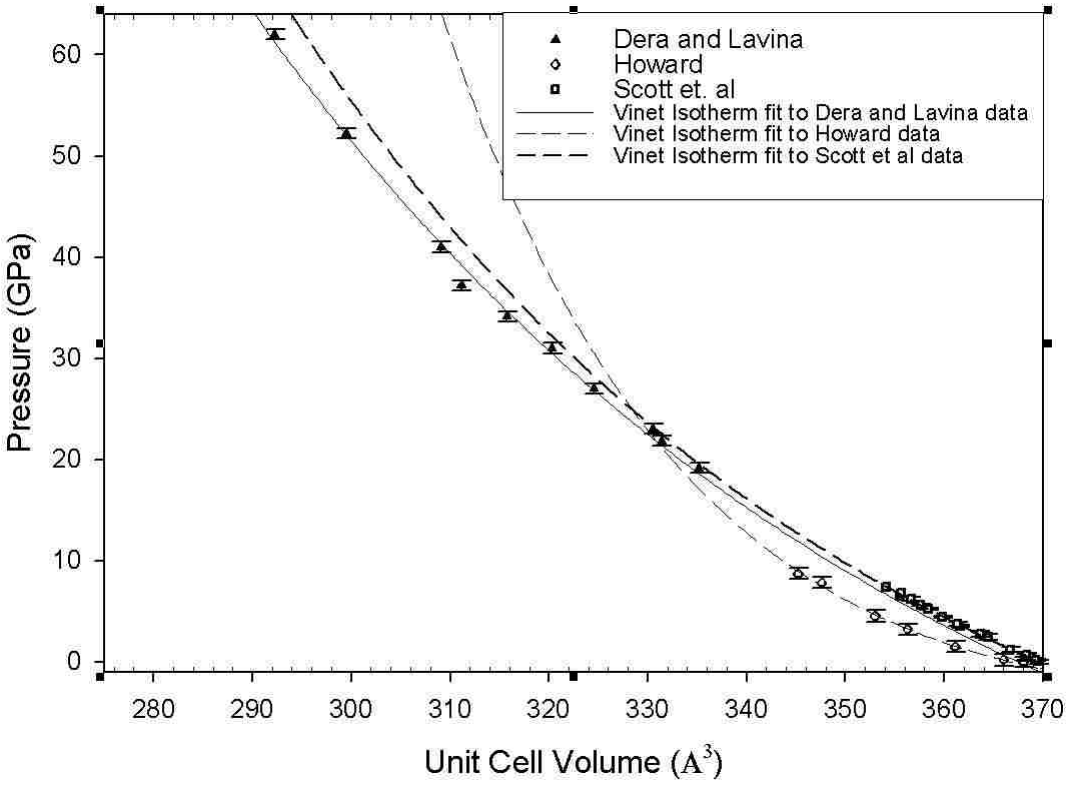

FIGURE 4.14: Compression data of Fe_3P from 3 independent research projects. The regressions were performed for data corresponding to hydrostatic conditions.

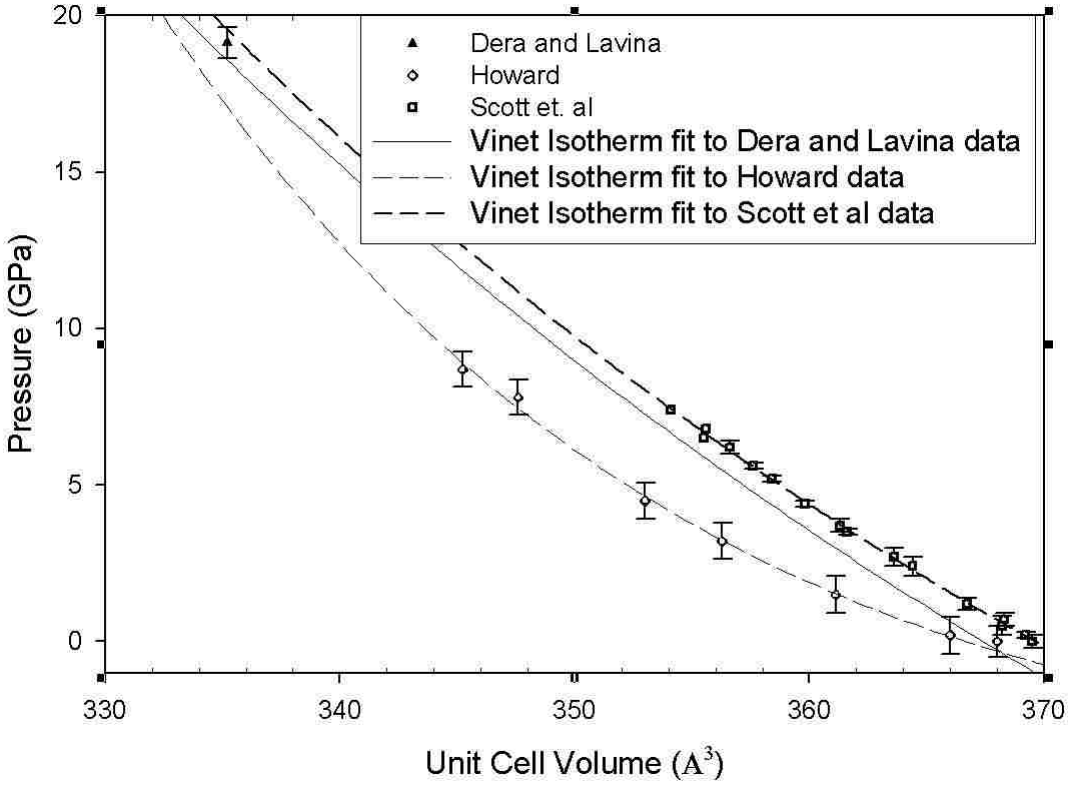

FIGURE 4.15: The above plot zoomed in for the hydrostatic pressure range for data collected in this project. There is good agreement between the fit and measured data.

Data Set	P_{ave} (GPa)	$\frac{\Delta c}{\Delta P}\frac{1}{c_{ave}}$ (1/GPa)	$\frac{\Delta a}{\Delta P}\frac{1}{a_{ave}}$ (1/GPa)
	0.10	5.5e-4	3.4e-3
Scott et al	0.35	2.2e-3	4.5e-3
	0.60	-1.1e-3	0.0
	0.95	3.1e-3	2.7e-3
	1.80	1.6e-3	2.3e-3
	2.55	2.6e-3	1.5e-3
	3.10	2.6e-3	1.9e-3
	3.60	2.8e-3	-2.3e-3
	4.05	1.4e-3	3.2e-3
	4.80	1.4e-3	2.0e-3
	5.40	2.5e-3	1.1e-3
	5.90	1.8e-3	7.5e-4
	6.35	2.9e-3	4.5e-3
	6.65	-7.4e-4	0.0
	7.10	2.2e-3	3.0e-3
	8.25	1.1e-3	1.2e-3
	9.30	4.4e-3	-2.3e-3
	9.70	1.7e-3	-3.4e-3
	9.95	-0.017	0.0388
	10.50	1.0e-3	9.1e-4
	11.65	2.1e-3	-8.8e-4
	12.35	5.6e-3	0.0183
	12.60	2.5e-3	4.6e-3
	13.20	2.4e-3	-3.1e-3
	14.05	-3.9e-3	0.0115
	15.00	5.5e-3	-0.0101
	16.10	2.9e-3	4.4e-3

TABLE 4.5: A table of the compressibilities of a and c calculated from the unit cell parameters determined from data collected by [27]. The ave subscript denotes the average between two adjacent data points, and Δ denotes their difference.

Fit Parameters		Vinet	3^{rd} order B-M
Howard	K_0 (GPa)	88 ± 14	81 ± 18
	K_0' (dimensionless)	18 ± 4	24 ± 9
	$V_0(\mathring{A})^3$	366.6 ± 0.9	366.8 ± 0.1
Dera and Lavina	K_0 (GPa)	74 ± 36	91 ± 46
	K_0' (dimensionless)	7.8 ± 1.6	7 ± 2
	$V_0(\mathring{A})^3$	389 ± 13	383 ± 12
Scott et al	K_0 (GPa)	155 ± 7	161 ± 11
	K_0' (dimensionless)	5.3 ± 2.1	7 ± 2
	$V_0(\mathring{A})^3$	369.6 ± 0.2	369.3 ± 0.4

TABLE 4.6: A table with the various K_0, K_0' and V_0 determined from each fit to corresponding data sets.

Iron Compound	K_0 (GPa)	K_0' (dimensionless)
FeS_2 [29]	155 ± 20	7.2 ± 0.1
Fe_2P (C22 phase) [30]	174 ± 7	4
Fe_2P (C23 phase) [30]	177 ± 3	4
Fe_3S [31]	170 ± 8	2.6 ± 0.5

TABLE 4.7: A table of K_0 and K_0' of similar iron compounds for comparison with synthetic Fe_3P. Fe_3S is a high pressure phase of FeS, and is of the same space group ($I\bar{4}$) as Fe_3P. Note that the various $K_0's$ generally agree within experimental uncertainty.

Fit Parameters	Vinet 2 par.	Vinet 3 par.	3^{rd} order B-M 2 par.	3^{rd} order B-M 3 par.
K_0 (GPa)	163 ± 14	155 ± 14	165 ± 12	162 ± 8
K_0' (dimensionless)	4.4 ± 0.6	4.6 ± 0.6	$4.3 \pm .4$	4.3 ± 0.6
$V_0(\mathring{A})^3$	368.0	368.0 ± 1.1	368	368.0 ± 1.1

TABLE 4.8: A table of results of various Vinet and Birch-Murnaghan fits to the data of [28] in conjunction with ambient pressure cell parameter data collected in this study. In the 2 parameter fits, V_0 is fixed and has small relative uncertainty compared to K_0 and K_0'. In the 3 parameter fits, V_0 is permitted to vary.

separately, as well as combined; we calculated K_0 using the equation

$$K_0 = \frac{1}{2s_{11} + s_{33}} \tag{4.2}$$

where s_{11} and s_{33} are the axial compressibilities of a and c at zero pressure.

Using the ambient pressure data for this study and that of [3], table 4.3 summarizes the results of K_0 and K_0' for the 2 and 3 parameter Vinet and Birch-Murnaghan isotherms.

Performing regressions on the data collected by [28] while constraining V_0, we find good agreement with that of [27] for the parameter K_0. Comparing the values of K_0 and K_0' to those of the iron-sulphide and iron-phosphide compounds in table 4.3, we also find good agreement. Although the values have relatively large error bars, these values of K_0 and K_0' appear much more realistic, and they agree within uncertainties. Performing these same regressions using an ambient pressure unit cell volume of $V_0 = 369.9(\mathring{A})^3$ [3] yielded very similar results, and agree well within uncertainties.

K_0 was also calculated from the axial compressibilities at zero pressure, which were calculated from fitting linear equations to the axial compressibility data in this study and that of [28]. By fitting a linear equation to each data set separately, we determined the s_{11} and s_{33} for each data set. Due to the large scatter in axial compressibility for cell parameter c for the data collected by [28], we could not reasonably constrain s_{33}. For this study we found that $s_{33} = 0.0032 \pm 0.0011$. The values for s_{11} are 0.0022 ± 0.0010 and 0.0024 ± 0.0010 for this study and [28] respectively. From this we calculate $K_0 = 104 \pm 31$ for this study. This value is much more reasonable than that

Fit Parameters	$K_0 = 104 \pm 31$ B-M	$K_0 = 104 \pm 31$ Vinet	$K_0 = 141 \pm 24$ B-M	$K_0 = 141 \pm 24$
K_0 (constr.)	104 ± 31,	104 ± 31	141 ± 24	141 ± 24
K_0 (vary)	164 ± 13	164 ± 13	163 ± 14	163 ± 14
K_0' (constr.)	9.9 ± 6.6	9.1 ± 3.5	5.8 ± 1.3	5.9 ± 1.1
K_0' (vary)	4.2 ± 0.5	4.4 ± 0.6	$4.2 \pm .5$	4.4 ± 0.6

TABLE 4.9: A table of results of various Vinet and Birch-Murnaghan fits to the data of [28] with K_0 implemented from axial compressibilities. In each fit, K_0 is both constrained and allowed to vary, V_0 is fixed at $368(\mathring{\text{A}})^3$. The "constr." and "vary" labels denote when K_0 was fixed and allowed to vary in the fit. For K_0', these labels denote whether K_0 was allowed to vary or was fixed.

presented in table 4.3. By combining data sets and performing linear regressions on the axial compressibilities, we find $s_{11} = 0.0018 \pm 0.0005$ and $s_{33} = 0.0035 \pm 0.0008$. This yields $K_0 = 141 \pm 24$, a value well in agreement with the determination from the Vinet and Birch-Murnaghan isotherm regressions when constraining V_0. Figures 4.3, 4.3 and 4.3 show the data and linear regression lines. Using the values of K_0 determined from the axial compressibility data, we again refine the parameters K_0 and K_0' in the Birch-Murnaghan and Vinet isotherms. Table 4.3 shows these results. We found that taking the K_0' values from table 4.3 and refining K_0 in the regressions, the results are self-consistent (K_0 values agree with one another within error).

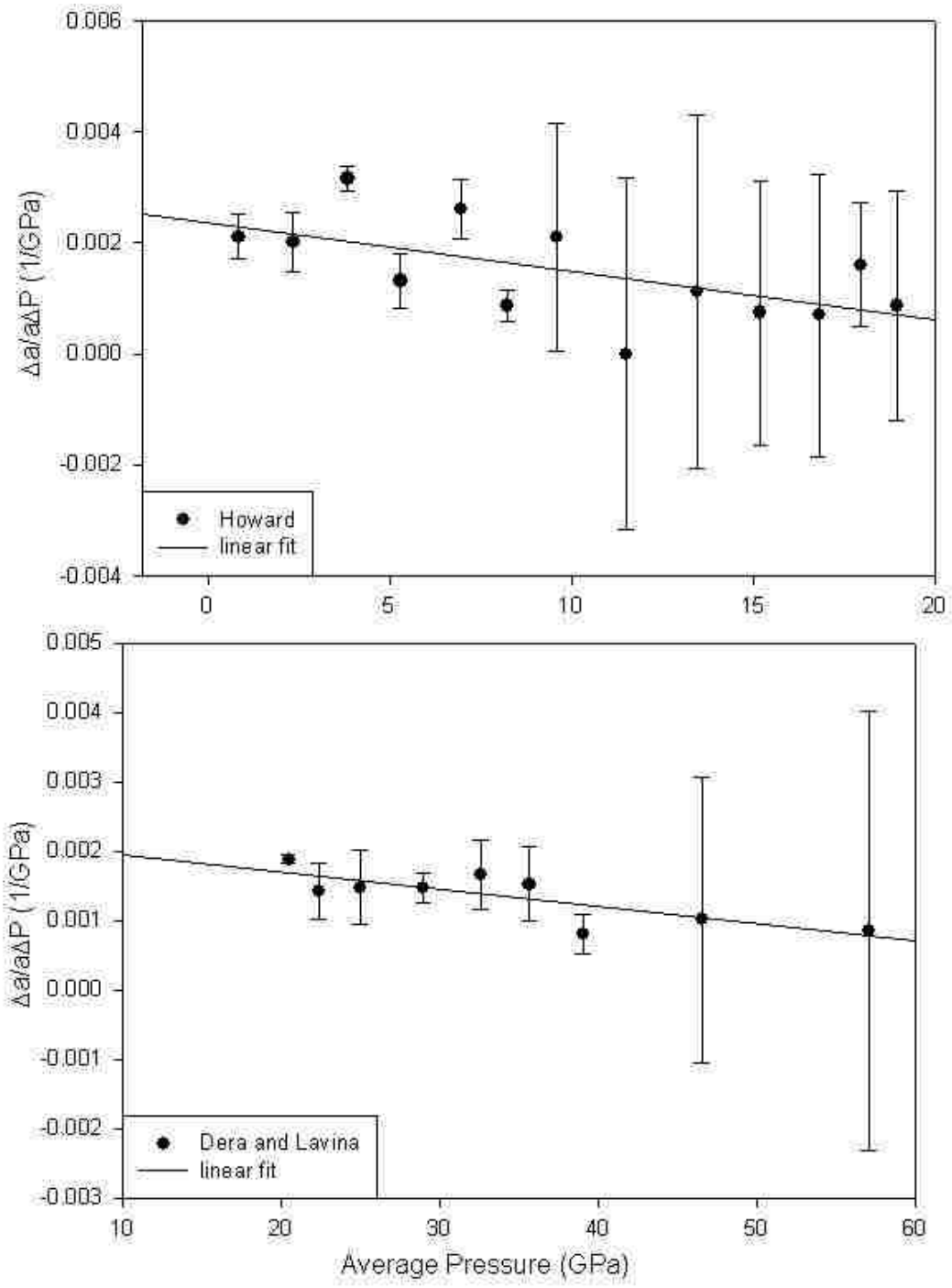

FIGURE 4.16: Linear fits of the axial compression of cell parameter a versus average pressure for data collected in this study and that of [28]. The severely outlying point ($P_{ave} = 0.1GPa$) is excluded from the fit. The compressibilities at $P = 0$ (s_{11}) are determined by the intercepts.

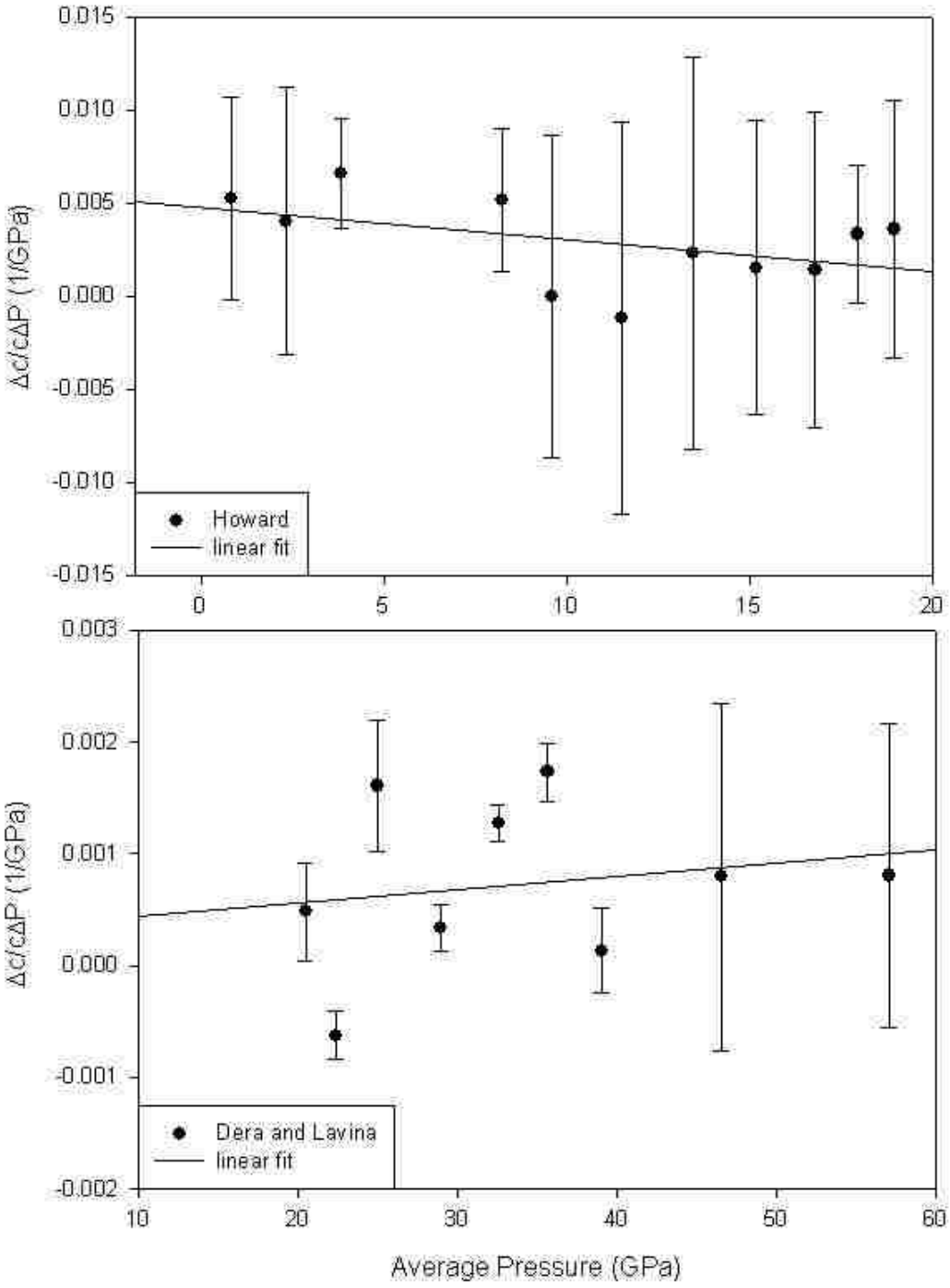

FIGURE 4.17: Linear fits of the axial compression of cell parameter C versus average pressure for data collected in this study and that of [28]. Severely outlying points ($P_{ave} = 0.1, 5.3, 6.95$) were excluded in the fit. The compressibilities at $P = 0$ (s_{33}) are determined by the intercepts.

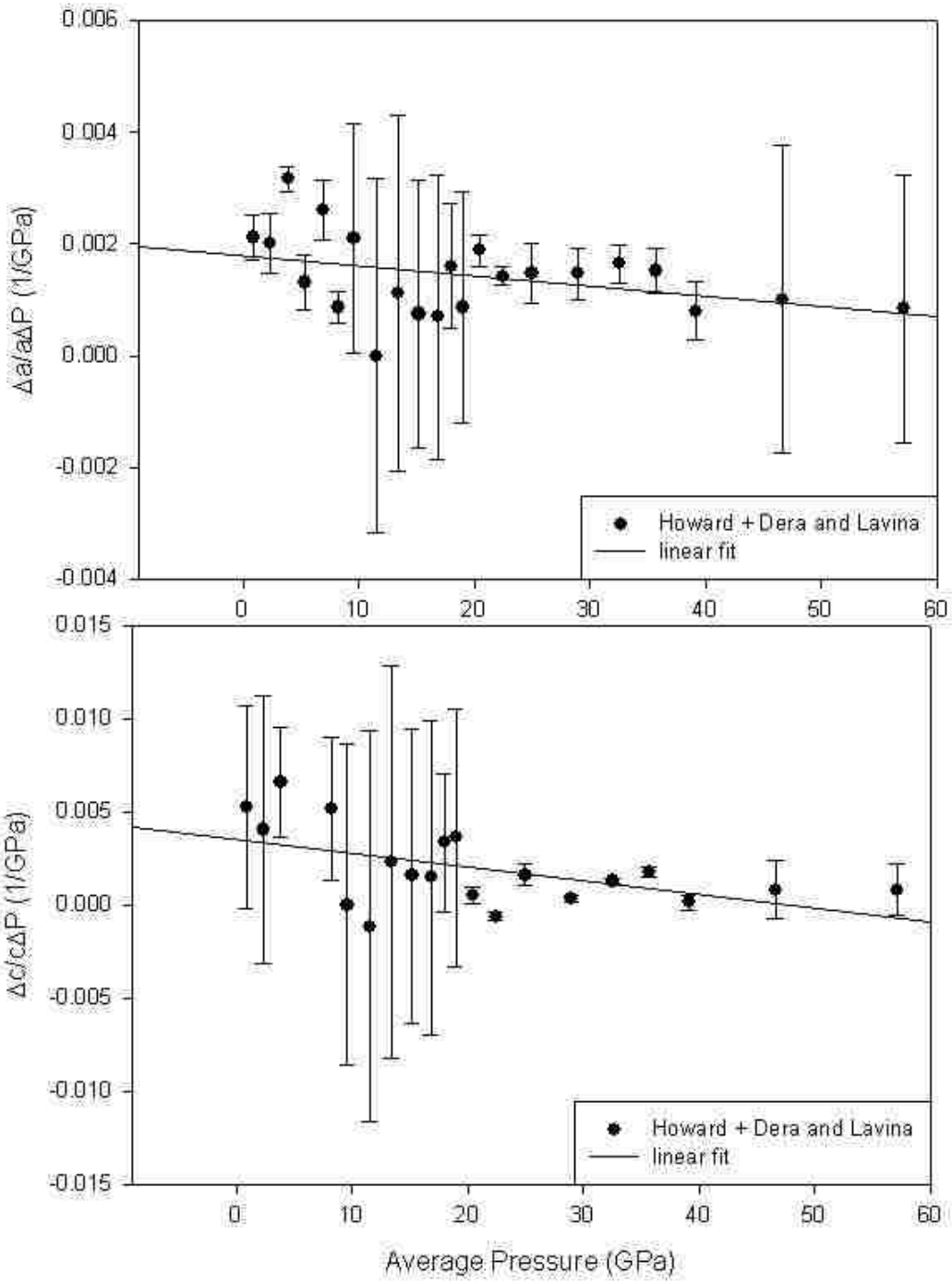

FIGURE 4.18: Linear fits to the combination of axial compressibility data collected in this study and that of [28]. The compressibilities (s_{11} and s_{33}) are determined by the intercepts.

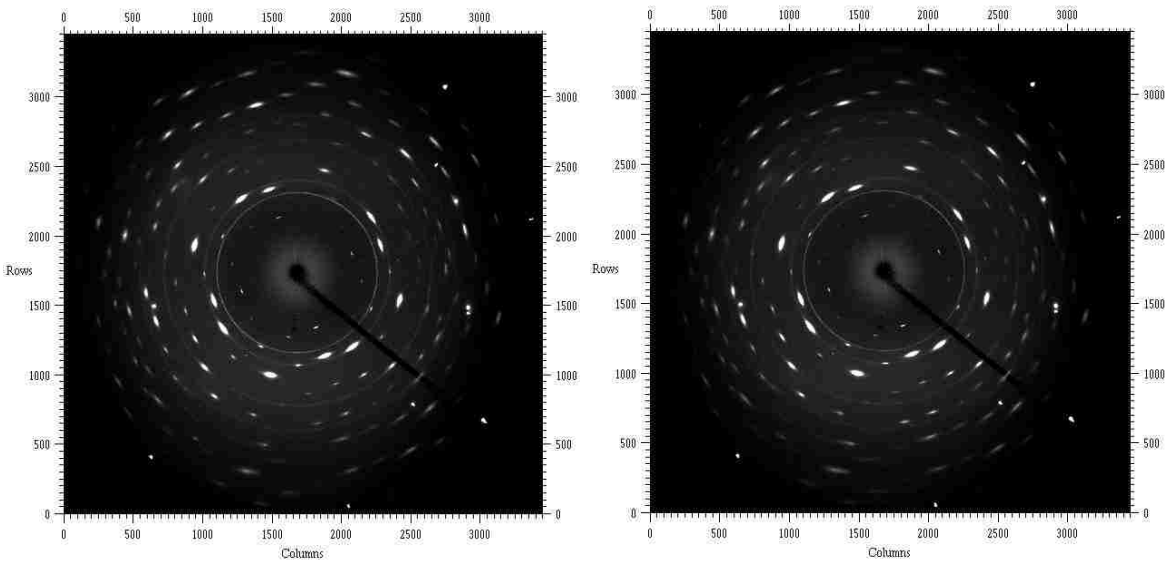

FIGURE 4.19: Diffraction patterns of strained Fe_3P at 30 GPa (left) and atmospheric pressure (right) after decompression. The broadening of the peaks remains after releasing pressure in the sample chamber.

4.4 Error Analysis

The accuracy to which the wavelength is known is essentially the accuracy to which the d-spacings can be measured. This corresponds to uncertainties on the order of $\sim 0.001(\mathring{\text{A}})$ in d. Neutron diffraction is sensitive enough to measure nuclear displacements, which are considerably smaller than $d-spacing$ uncertainty. In x-ray diffraction experiments, x-rays interact with electrons, which form a cloud making up the volume of atom. Since the wavelength used is much larger than atomic displacements, main source of uncertainty is due to the bandwidth in λ and/or the point spread in the detector.

Uncertainties were estimated using the spread in λ and the error propagation formula 4.3. Like reflections (reflections with same d-spacing but different (x, y) coordinates) under hydrostatic conditions differed by no more than $0.001(\mathring{\text{A}})$. This corresponded to an uncertainty of $\Delta(2\vartheta) = 0.08^\circ$ assigned to each reflection. Using the general propagation of errors formula [32]

$$(\delta f)^2 = \sum_i \left(\frac{\partial f}{\partial x_i}\right)^2 (\delta x_i)^2 \tag{4.3}$$

we calculated the error on $\frac{1}{d^2}$ is calculated as

$$\frac{1}{d^2} = \frac{\sin^2\theta}{\lambda^2} \tag{4.4}$$

$$\sigma^2_{\frac{1}{d^2}} = \left(\frac{2\sin\theta\cos\theta}{\lambda^2}\right)^2 \sigma^2_\theta + \left(\frac{2\sin^2\theta}{\lambda^3}\right)^2 \sigma^2_\lambda \tag{4.5}$$

$$\sigma_{\frac{1}{d^2}} = \frac{\sin 2\theta}{\lambda^2}\sqrt{\sigma^2_\theta + \left(\frac{\sigma_\lambda}{\lambda}\right)^2 \tan^2\theta}. \tag{4.6}$$

These were the weights used for the regression of $\frac{1}{d^2}$ versus $\frac{h^2+k^2}{a^2} + \frac{l^2}{c^2}$. From the fit we obtained the cell parameters and there respective uncertainties. The error propagation formula was used for the error in the unit cell volume $V = a^2c$ to obtain

$$\sigma_V = \sqrt{4a^2c^2\sigma_a^2 + a^4\sigma_c^2} \tag{4.7}$$

The error propagation formula was applied to each calculated quantity in the analysis.

CHAPTER 5

DISCUSSION AND CONCLUSIONS

Based on the x-ray diffraction data obtained at Sector 16-IDB of the Advanced Photon Source, and that of independent data, we conclude that no apparent phase transition is observed in single crystal Fe_3P at room temperature up to 8.7 GPa. Analysis of the pressure versus unit cell volume isotherms and axial compressibilities for data collected under hydrostatic conditions do not indicate that any structural phase transitions occur in this material up to 62 GPa.

Performing Vinet and Birch-Murnaghan regressions on the data collected by [28], in conjunction with the ambient pressure data point, we find good agreement betweeen K_0 and K_0' between each regression. These results also agree well with those of [27], and the iron compounds presented in table 4.3. It was shown that if we do not impose the ambient pressure unit cell volume in the refinement of the high pressure data alone, we obtain unreasonable results for K_0, K_0' and V_0 in the Vinet and B-M regressions. This is due to extrapolation over a very large range, where the fit parameters may vary significantly to fit the data, yielding unreliable results.

The values of K_0 and K_0' determined in this analysis suggests that the compression behavior of Fe_3P and Fe_3S is determined mainly by the cation. A comparison of K_0 and K_0' for Fe_3P and Fe_3S yield the same result for K_0 (within uncertainty) and a similar value for K_0'. This suggests that changing the anion has a small effect on the compression behavior. Unfortunately, no literature on the compression behavior of Ni_3P current exist, thus this comparison could not be made.

The ambient pressure unit cell volumes for Fe_3P and Ni_3P suggest that the unit cell volume is also determined mainly by the cation. By replacing Fe with Ni in the compound, we find marked differences in unit cell parameters, although the ratio a/c remains the same. This is due to the type of bonding as well as the bonding radii for these compounds.The metallic radius of nickel ($124pm$) is smaller than that of

iron ($126pm$) [33]. The fact that Ni_3P has uniformly smaller unit cell parameters suggests that the bonding in these compounds is more metallic/covalent and less ionic, although there may be some ionic contributions.

Performing a triclinic regression on the data gives slight disagreement with what one would expect for a tetragonal lattice. If the lattice is truly tetragonal, one should find that the angles α, β and γ are 90° within experimental uncertainties, assuming sufficient statistics in the diffraction patterns. The data also suggest that any previous strains sustained by the sample can be observed by recording its x-ray diffraction pattern (assuming the sample is a single crystal). Assuming the structure of meteoritic schreibersite, $(Fe, Ni)_3P$, behaves similarly to the structurally equivalent synthetic Fe_3P as a function of pressure, a diffraction analysis of the sample will yield information on the previous stresses sustained.

Clearly, there is a marked difference in the measured values for cell parameter c in this experiment as compared with that of [27]. We do not observe a large disagreement (within two standard deviations) between c under ambient conditions between this study and that of [27, 26], so we do not assume that the crystal was significantly strained along the c-axis prior to experiment. If the crystal was previously compressed/strained along the c-axis, it would remain strained, thus decreasing the value of this parameter, as was shown in this study. One study [3] showed that the crystal perfection of schreibersite depends on its history, and in general is totally elastically strained.

The statistics for cell parameter c were relatively poor compared to a. Roughly half of the reflections in each pattern belong to the $hk0$ zone, the other half belonging to the $hk1$ zone. The cell parameter c was determined with large uncertainty in the fit $\frac{1}{d^2} = \frac{h^2+k^2}{a^2} + \frac{l^2}{c^2}$, as c is arbitrary for $hk0$ reflections, and the $hk1$ zone yields limited information (small sampling of l-direction in reciprocal space). Comparing to literature values for c (presented in the previous chapter), we find an offset of

$\sim 0.03(\text{Å})$ below the expected value. For more reliable results, one would like to sample d-spacings corresponding to many points spread out in reciprocal space, which would give a better overall representation of the reciprocal lattice. In the case of this study only the $hk0$ and $hk1$ nets were sampled, and c is poorly represented by these statistics.

The source of the unphysical behavior of cell parameter c at 6 GPa is due to an unidentified error in the regression. Cell parameter a agrees with that of [27] and [28] at this pressure, and this anomaly in c is not considered critical phenomena. Interestingly, d-spacings for all reflections at this pressure are all less than the d-spacings at lower pressures, and larger for higher pressures. This behavior is expected, as the d-spacings between atomic planes should decrease as pressure increases. Contrary to expectation, a regression of $\frac{1}{d^2} = \frac{h^2+k^2}{a^2} + \frac{l^2}{c^2}$ for this diffraction pattern yields $c = 4.63$, a value larger than at atmospheric pressure. The source of this error was not identified; regression in both sigmaplot and Unit-cell return similar values (agree within errors) of the cell parameters, including the triclinic regressions as well. The source of error for this data point could not be accounted for, thus the information for c at this pressure cannot be included for the analysis of the axial/bulk properties of the material.

Around 10 GPa, the 4:1 methanol:ethanol pressure medium begins to harden, and pressures within the sample chamber are no longer hydrostatic. This is observed in the diffraction patterns above 10 GPa: peaks become distorted and broadened, the various $\pm h \pm k \pm l$ reflection d-spacings for like reflections have larger disagreements with each other, and the crystal structure may no longer be considered a lattice. The stiffening of the pressure medium causes an apparent stiffness in the sample, thus we observe small changes in a and c near this pressure. We notice that the cell parameters a and c change very little with increasing pressure around 10 GPa, but above this pressure, cell parameters a and c appear to soften again. In the non-

hydrostatic regime, a and c appears to be harder compared to hydrostatic data. In the non-hydrostatic regime, unit cell parameters are no longer reasonably uniform over the sample, and a P-V isothermal relationship is not a valid description of the sample behavior.

Besides the data collected by [27], there are no profoundly abrupt changes in the axial compressibilities, as shown by figures 4.3 and 4.3, outside of uncertainties. It appears that the compressibilities remain constant up to 62 GPa; in both the hydrostatic and non-hydrostatic regimes of this experiment, the axial compressibilities versus average pressure do not significantly deviate from a linear relationship outside of uncertainties.

As pressure is relieved, we observe, from the diffraction pattern, that the sample remains in this strained state. There is no evidence of crystal twinning in the diffraction patterns over the measured pressure range. The peaks remain highly broadened and d-spacings remain very uncertain after full decompression. From this we assume that similar deformations present in meteoritic $(Fe, Ni)_3P$ yield evidence of previously sustained deformations due to anisotropic stress/strain caused by compression and/or extreme temperature environments. Meteorites, from initial formation to human contact, undergo many extreme processes which can permanently effect the crystalline structure of constituent elemental compounds. The state of the crystal also yields information about the environment in which it existed.

Looking at the axial compressibilities as a function of pressure, we found a reasonable linear agreement for the data collected in this study (aside from one outlying point) and that of [28]. We do not find linear relationships for the data collected by [27], but erratic deviation in the axial compressibility. Performing a linear weighted least squares fit to the data collected in this study and that of [28] allowed us to determine the axial compressibility of cell parameter a at zero pressure. Combining the data and performing the linear regression gave us the most accurate

result for s_{11}.

As for cell parameter c, we observe quite erratic behavior for data collected in this study and that of [27], in addition to relatively large uncertainties. Fitting a linear equation to the data collected in this study allowed for a crude estimation of s_{3333}. We could not reasonably calculate this value for the data collected by [28] as the extrapolation range was too large considering the spread in axial compressibility over the measured pressure range. This does not allow us to constrain the axial compressibility along c at zero pressure, thus we get a large error for this value. Combining the data collected in this study and that of [28] gave the most accurate result for s_{33}.

By calculating s_{11} and s_{33}, we estimated K_0, and obtained a more reasonable result than from the 3 parameter Vinet fit. The uncertainties is the various axial compressibilities are relatively large, and linear fits to the data are relatively uncertain. The value of K_0 obtained from this analysis should not be considered accurate, but is mildly approximate. In addition, this value can be implemented into an isotherm regression as an initial guess for refinement; this will likely yield more reliable results. In order to obtain more reliable results for the axial compressibilities, one must make measurements in smaller pressure increments.

It appears that the work of [28] gives the most reliable results. There is no evidence in the diffraction pattern of significant deviatoric stress up to 62 GPa; this is the result of using a helium pressure medium. This study and the work of [27] used a methanol/ethanol pressure medium, thus results above 10 GPa are not reliable. Also, the compressibility in the cell parameter c calculated in this study (outside of anomalous region) agrees with that of [28], although uncertainties are very large.

The study performed by [27] used a polycrystalline aggregate (or powder), whereas the data collected in this study and by [28] used single crystal samples. When milling single crystals of Fe_3P into a fine grained powder, one induces strain in the various

crystallites, and the powder diffraction rings are highly broadened due to strain. In addition, a polycrystalline or powdered sample contains many smaller crystals; when loaded and compressed in a diamond anvil cell, the individual crystals are pressed against each other, causing anisotropic strain over the sample volume. This causes asymmetric broadening along the powder diffraction rings, as the crystallites are randomly oriented and strained. This non-uniformity cannot be resolved using powder diffraction. The angular integration of these distorted rings gives an overall average of all contributions. This likely accounts for the deviating nature of the axial compressibilities as a function of average pressure for this data set.

REFERENCES

[1] V. V. Nemoshkalenko, N. A. Tomashevskii, V. B. Chernogorenko, and L. Y. Solomatina, "Mossbauer spectroscopy of iron phosphide powders," *Poroshk. Metall.*, vol. 229, no. 1, pp. 57–61, 1982.

[2] I. M. Fedorchenko, G. M. Derkacheva, and I. I. Panaioti, "Effect of phosphorus on the friction properties of a material based on alloyed iron," *Poroshk. Metall.*, no. 11, pp. 99–101, 1969.

[3] V. Geist, G. Wagner, G. Nolze, and O. Moretzki, "Investigations of the meteoritic mineral $(Fe, Ni)_3P$," *Cryst. Res. Technol.*, vol. 40, no. 1/2.

[4] S. Rundquist *Acta Chem. Scand.*, vol. 16, p. 1, 1962.

[5] B. Aronsson *Acta Chem. Scand.*, vol. 9, p. 138, 1955.

[6] D. Schroeder, *An Introduction to Thermal Physics.* Addison Wesley Longman, (68,180) 2000.

[7] F. Birch, "Finite elastic strain of cubic crystals," *Physical Review*, vol. 71, no. 11, pp. 809–824, 1947.

[8] P. Coles and F. Lucchin, *Cosmology: The Origin and Evolution of Cosmic Structure.* Wiley, (169) 2002.

[9] L. Landau and E. Lifshitz, *Quantum Mechanics, 3rd Edition*, vol. 3. Butterworth-Heinemann, 1958.

[10] F. D. Murnaghan, "Finite deformations of an elastic solid," *(Wiley, New York)*, 1951.

[11] P. Vinet, J. Ferrante, J. Smith, and J. H. Rose, "A universal equation of state for solids," *J. Phys. C: Solid State Phys.*, vol. 19, pp. L467–L473, 1986.

[12] M. F. C. Ladd and R. A. Palmer, *Structure Determination by X-ray Crystallography.* Plenum Press, (73-77) 1977.

[13] L. Landau and E. Lifshitz, *Statistical Physics, 3rd Edition Part 1*, vol. 5. Butterworth-Heinemann, (413-416) 1951.

[14] A. C. Melissinos and J. Napolitano, *Experiments in Modern Physics.* Academic Press, (367-383) 2003.

[15] L. Dubrovinsky1, S. Saxena, N. Dubrovinskaia, S. Rekhi, and T. L. Bihan, "Gruneisen parameter of iron up to 300 gpa from in-situ x-ray study," *American Mineralogist*, vol. 85, no. 2.

[16] K. Takemura, "Evaluation of the hydrostaticity of a helium-pressure medium with powder x-ray diffraction techniques," *J. Appl. Phys.*, vol. 89, p. 662, 2001.

[17] R. J. Angel, M. Bujak, J. Zhao, G. D. Gatta, and S. D. Jacobsen, "Effective hydrostatic limits of pressure media for high-pressure crystallographic studies," *Journal of Applied Crystallography*, vol. 40, pp. 26–32, 2007.

[18] I. F. Silvera, A. D. Chijioke, W. J. Nellis, A. Soldatov, and J. Tempere, "Calibration of the ruby pressure scale to 150 gpa," *Physica Status Solidi B Basic Research*, vol. 244, no. 1, pp. 460–467, 2007.

[19] A. Dewaele, P. Loubeyre, and M. Mezouar, "Equations of state of six metals above 94 gpa," *Physical Review B*, vol. 70, p. 094112, 2004.

[20] K. Takemura and A. Dewaele, "Isothermal equation of state for gold with a He-pressure medium," *Physical review B*, vol. 78, p. 104119, 2008.

[21] M. I. Eremets, *High Pressure Experimental Methods*. Oxford Science, 1997.

[22] A. P. Hammersley, S. Svensson, M. Hanfland, and D. Hausermann, "Two-dimensional detector software: From real detector to idealised image or two-theta scan," *High Pressure Res.*, pp. 235–238, 1996.

[23] *sigmaplot*. Systat Software Inc., 8.0 ed., 2005.

[24] Stanislav Sinogeikin, personal communication.

[25] T. Holland and S. Redfern, "Unit cell refinement from powder diffraction data: the use of regression diagnostics," *Mineralogical Magazine*, vol. 61, pp. 65–77, 1997.

[26] Joint Committee on Powder Diffraction Standards, card 00-019-0617.

[27] H. P. Scott, S. Huggins, M. R. Frank, S. J. Maglio, C. D. Martin, Y. Meng, J. Santillan, and Q. Williams, "Equation of state and high-pressure stability of Fe_3P-schreibersite: Implications for phosphorus storage in planetary cores," *Geophysical Research Letters*, vol. 34, p. L06302, 2007.

[28] Przymek Dera and Barbara Lavina, personal communication.

[29] N. Benbattouche, G. A. Saunders, E. F. Lambson, and W. Honle, "The dependences of teh elastic stiffness moduli and the poisson ratio of natural iron pyrites FeS_2 upon pressure and temperature," *J. Phys. D: Appl. Phys.*, vol. 22, pp. 670–675, 1989.

[30] P. Dera, B. Lavina, L. A. Borkowski, V. B. Prakapenka, S. R. Sutton, M. L. Rivers, R. T. Downs, N. Z. Boctor, and C. T. Prewitt, "High-pressure polymorphism of Fe_2P and its implications for meteorites and earth's core," *Geophysical Research Letters*, vol. 35, p. L10301, 2008.

[31] Y. Fei, J. Li, C. M. Bertka, and C. T. Prewitt, "Structure type and bulk modulus of Fe_3S, a new iron-sulfur compound," *American Mineralogist*, vol. 85, pp. 1830–1833, 2000.

[32] L. Lyons, *A Practical Guide to Data Analysis for Physical Science Students*. Cambridge University Press, (73) 1991.

[33] N. N. Greenwood and A. Earnshaw, *Chemistry of the Elements*. Oxford: Butterworth-Heinemann, (326-328) 1997.

VITA

Graduate College
University of Nevada, Las Vegas

John W. Howard

Degrees:
Bachelor of Sciences, Physics, 2007
University of Nevada, Las Vegas

Thesis Title: Finite Strain Studies of Single Crystal Fe_3P Under High Pressures

Thesis Examination Committee:
Chairperson, Dr. Lon Spight
Co-Chairperson, Dr. Oliver Tschauner
Committee Member, Dr. Michael Pravica
Graduate Faculty Representative, Dr. Adam Simon